The nature of the TRAPPIST-1 exoplanets

Simon L. Grimm[1], Brice-Olivier Demory[1], Michaël Gillon[2], Caroline Dorn[1,19], Eric Agol[3,4,17,18], Artem Burdanov[2], Laetitia Delrez[5,2], Marko Sestovic[1], Amaury H.M.J. Triaud[6,7], Martin Turbet[8], Émeline Bolmont[9], Anthony Caldas[10], Julien de Wit[11], Emmanuël Jehin[2], Jérémy Leconte[10], Sean N. Raymond[10], Valérie Van Grootel[2], Adam J. Burgasser[12], Sean Carey[13], Daniel Fabrycky[14], Kevin Heng[1], David M. Hernandez[15], James G. Ingalls[13], Susan Lederer[16], Franck Selsis[10], Didier Queloz[5]

[1] University of Bern, Center for Space and Habitability, Gesellschaftsstrasse 6, CH-3012, Bern, Switzerland
[2] Space Sciences, Technologies and Astrophysics Research (STAR) Institute, Université de Lège, Allée du 6 Août 19C, B-4000 Liège, Belgium
[3] Astronomy Department, University of Washington, Seattle, WA, 98195, USA
[4] NASA Astrobiology Institute's Virtual Planetary Laboratory, Seattle, WA, 98195, USA
[5] Cavendish Laboratory, J J Thomson Avenue, Cambridge, CB3 0HE, UK
[6] Institute of Astronomy, Madingley Road, Cambridge CB3 0HA, UK
[7] School of Physics & Astronomy, University of Birmingham, Edgbaston, Birmingham B15 2TT, United Kingdom.
[8] Laboratoire de Météorologie Dynamique, IPSL, Sorbonne Universités, UPMC Univ Paris 06, CNRS, 4 place Jussieu, 75005 Paris, France
[9] Université Paris Diderot, AIM, Sorbonne Paris Cité, CEA, CNRS, F-91191 Gif-sur-Yvette, France.
[10] Laboratoire d'astrophysique de Bordeaux, Univ. Bordeaux, CNRS, B18N, allée Geoffroy Saint-Hilaire, 33615 Pessac, France
[11] Department of Earth, Atmospheric and Planetary Sciences, Massachusetts Institute of Technology, 77 Massachusetts Avenue, Cambridge, MA 02139, USA
[12] Center for Astrophysics and Space Science, University of California San Diego, La Jolla, CA, 92093, USA
[13] IPAC, Mail Code 314-6, Calif. Inst. of Technology, 1200 E California Blvd, Pasadena, CA 91125, USA
[14] Department of Astronomy and Astrophysics, Univ. of Chicago, 5640 S Ellis Ave, Chicago, IL 60637, USA
[15] Department of Physics and Kavli Institute for Astrophysics and Space Research, Massachusetts Institute of Technology, 77 Massachusetts Ave., Cambridge, Massachusetts 02139, USA
[16] NASA Johnson Space Center, 2101 NASA Parkway, Houston, Texas, 77058, USA
[17] Guggenheim Fellow
[18] Institut d'Astrophysique de Paris, 98 bis bd Arago, F-75014 Paris, France
[19] University of Zurich, Institute of Computational Sciences, Winterthurerstrasse 190, CH-8057, Zurich, Switzerland

ABSTRACT

Context. The TRAPPIST-1 system hosts seven Earth-sized, temperate exoplanets orbiting an ultra-cool dwarf star. As such, it represents a remarkable setting to study the formation and evolution of terrestrial planets that formed in the same protoplanetary disk. While the sizes of the TRAPPIST-1 planets are all known to better than 5% precision, their densities have significant uncertainties (between 28% and 95%) because of poor constraints on the planet's masses.
Aims. The goal of this paper is to improve our knowledge of the TRAPPIST-1 planetary masses and densities using transit-timing variations (TTV). The complexity of the TTV inversion problem is known to be particularly acute in multi-planetary systems (convergence issues, degeneracies and size of the parameter space), especially for resonant chain systems such as TRAPPIST-1.
Methods. To overcome these challenges, we have used a novel method that employs a genetic algorithm coupled to a full N-body integrator that we applied to a set of 284 individual transit timings. This approach enables us to efficiently explore the parameter space and to derive reliable masses and densities from TTVs for all seven planets.
Results. Our new masses result in a five- to eight-fold improvement on the planetary density uncertainties, with precisions ranging from 5% to 12%. These updated values provide new insights into the bulk structure of the TRAPPIST-1 planets. We find that TRAPPIST-1 c and e likely have largely rocky interiors, while planets b, d, f, g, and h require envelopes of volatiles in the form of thick atmospheres, oceans, or ice, in most cases with water mass fractions less than 5%.

Key words. Planets and satellites – Techniques: photometric – Methods: numerical

1. Introduction

The TRAPPIST-1 system, which harbours seven Earth-size exoplanets orbiting an ultra-cool star (Gillon et al. 2017), represents a fascinating setting to study the formation and evolution of tightly-packed small planet systems. While the TRAPPIST-1 planet sizes are all known to better than 5%, their densities suffer from significant uncertainty (between 28 and 95%) because of loose constraints on planet masses. This critically impacts in turn our knowledge of the planetary interiors, formation pathway (Ormel et al. 2017; Unterborn et al. 2017) and long-term stability of the system. So far, most exoplanet masses have been

measured using the radial-velocity technique. But because of the TRAPPIST-1 faintness (V=19), precise constraints on Earth-mass planets are beyond the reach of existing spectrographs.

Thankfully, the resonant chain formed by the planetary septet (Luger et al. 2017) dramatically increases the exchange of torque at each planet conjunction, resulting in transit timing variations (TTV) (Holman 2005; Agol et al. 2005) that are well above our demonstrated noise limit for this system. Presently, the TTV approach thus represents the only avenue to characterise the physical properties of the system. The TRAPPIST-1 system shows dynamical similarities to Kepler-90 system (Cabrera et al. 2014) which contains also seven planets and resonances conditions between pairs of the them.

Planetary masses published in the TRAPPIST-1 discovery paper (Gillon et al. 2017) were bearing conservative uncertainties because the different techniques used by the authors suggested a non-monotonous parameter space with the absence of a single global minimum. Subsequent studies have adequately invoked the requirement for long-term stability to refine these masses further (Quarles et al. 2017; Tamayo et al. 2017a), but the parameter space allowed by this additional constraint may still be too large to precisely identify the planet physical properties. The recent K2 observations of TRAPPIST-1 (Luger et al. 2017) enabled another team to compute updated masses for the system using the K2 data combined to archival data (Wang et al. 2017). Their approach relies on the TTVFast algorithm (Deck et al. 2014), which uses low-order symplectic co-ordinates and an approximate scheme for finding transit times to increase efficiency. It is however unclear from that paper how the correlations between parameters are taken into account and how comprehensive the search of the parameter space is. Only a full benchmarking of this approach with more accurate integrators for this specific system could validate their results.

In the present paper, we have used a novel approach that combines an efficient exploration of the parameter space based on a genetic algorithm with an accurate N-body integration scheme. The associated complexity being compensated by more computing resources. The philosophy of this approach could be considered 'brute force' but still represents a useful avenue to appreciate the degeneracy of the problem without doubting the accuracy of the numerical integration scheme.

2. Observations

2.1. Published data

This study is based on 284 transit timings obtained between September 17, 2015 and March 27, 2017 through the TRAPPIST and SPECULOOS collaboration. The input data for our transit-timing analysis includes 107 transits of planet b, 72 of c, 35 of d, 28 of e, 19 of f, 16 of g and 7 of h. In addition to the TRAPPIST-1 transit timings already presented in the literature (Gillon et al. 2016, 2017; de Wit et al. 2016; Luger et al. 2017), we have included new data from the *Spitzer Space Telescope* (PID 12126, 12130 and 13067) and from *Kepler and K2* (PID 12046). Transit timing uncertainties range from 8 sec to 6.5 min with a median precision across our dataset of 55 sec. The analysis of the K2 data is presented below while the new Spitzer data obtained between February and March 2017 are presented in a separate publication (Delrez et al. 2018). We include the full list of transit timings used in this work in Tables A.1 through A.10 of Appendix A.

2.2. K2 short-cadence photometry

For the purpose of this analysis we have included the transit timings derived from the K2 photometry (Howell et al. 2014), which observed TRAPPIST-1 during Campaign 12 (Luger et al. 2017). We detail in the following the data reduction of this dataset. We used the K2's pipeline-calibrated short-cadence target pixel files (TPF) that includes the correct timestamps. The K2 TPF TRAPPIST-1 (EPIC ID 246199087) aperture is a 9x10 postage stamp centred on the target star, with 1-minute cadence intervals. We performed the photometric reduction by applying a centroiding algorithm to find the (x, y) position of the PSF centre in each frame. We used a circular top-hat aperture, centred on the fitted PSF centre of each frame, to sum up the flux. We find this method to produce a better photometric precision compared to apertures with fixed positions.

The raw lightcurve contains significant correlated noise, primarily from instrumental systematics due to *K2*'s periodic roll angle drift and stellar variability. We have accounted for these systematic sources using a Gaussian-processes (GP) method, relying on the fact that the instrumental noise is correlated with the satellite's roll angle drift (and thus also the (x, y) position of the target) and that the stellar variability has a much longer timescale than the transits. We used an additive kernel with separate spatial, time and white noise components (Aigrain et al. 2015, 2016; Luger et al. 2017):

$$k_{xy}(x_i, y_i, x_j, y_j) = A_{xy} \exp\left[-\frac{(x_i - x_j)^2}{L_x^2} - \frac{(y_i - y_j)^2}{L_y^2} \right] \qquad (1)$$

$$k_{xy}(t_i, t_j) = A_t \exp\left[-\frac{(t_i - t_j)^2}{L_t^2} \right] \qquad (2)$$

$$K_{ij} = k_{xy}(x_i, y_i, x_j, y_j) + k_t(t_i, t_j) + \sigma^2 \delta_{ij}, \qquad (3)$$

where x and y are the pixel co-ordinates of the centroid, t is the time of the observation, and the other variables (A_{xy}, L_x, L_y, A_t, L_t, σ) are hyperparameters in the GP model (Aigrain et al. 2016). We used the GEORGE package (Ambikasaran et al. 2016) to implement the GP model. We used a differential evolution algorithm (Storn & Price 1997) followed by a local optimisation to find the maximum-likelihood hyperparameters.

We optimised the hyperparameters and detrended the lightcurve in three stages. In each stage, using the hyperparameter values from the previous stage (starting with manually chosen values), we fitted the GP regression and flag all points further than 3σ from the mean as outliers. The next GP regression and hyperparameter optimisation is performed by excluding the outlier values. Points in and around transits are not included in the fit. Due to the large numbers of points in the short cadence lightcurve, only a random subset of the points is used to perform each detrending and optimisation step to render the computation less intensive. We achieved a final RMS of 349 ppm per 6 hours (excluding in-transit points and flares). Out of the entire dataset, we discarded only two transits because of a low SNR at the following BJD$_{TDB}$: 7795.706 and 7799.721. Both eclipses correspond to transits of planet d.

We then used a Markov Chain Monte Carlo (MCMC) algorithm previously described in the literature (Gillon et al. 2012) to derive the individual transit timings of TRAPPIST-1b, c, d, e, f, g, and h from the detrended K2 light curve. Each photometric data point is attached to a conservative error bar that accounts for
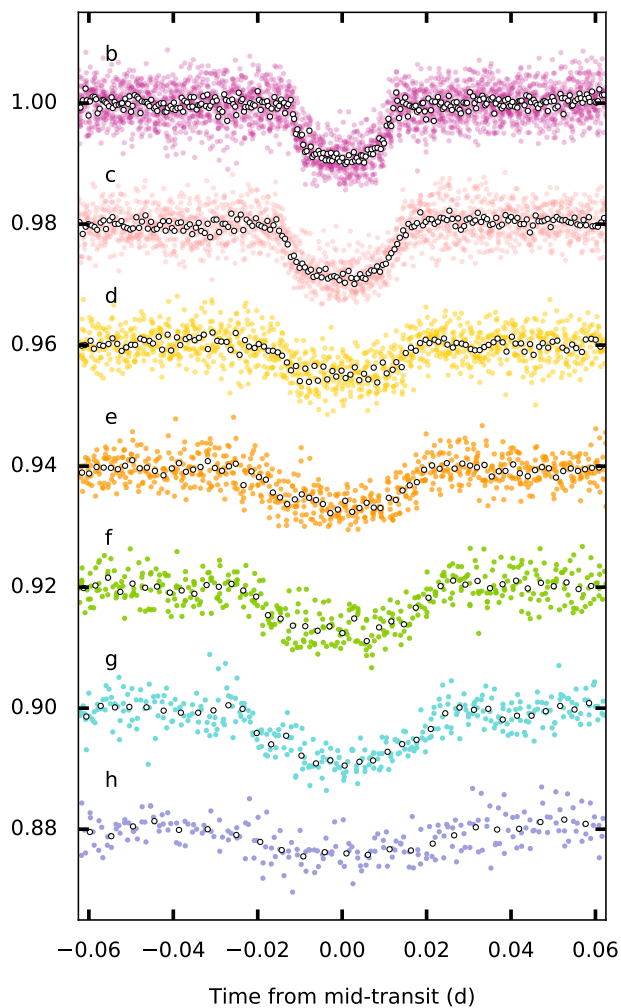
Fig. 1. Folded short-cadence lightcurves extracted from K2 data, corrected for their TTVs. For clarity, the short-cadence data are binned to produce the coloured points, with five cadences per point. The white points are further binned, with ten points taken from the folded curve per bin.

the uncertainties in the detrending process presented above. We have imposed normal priors in the MCMC fit on the orbital period, transit mid-time centre and impact parameter for all planets to the published values (Gillon et al. 2017). We computed the quadratic limb-darkening coefficients u_1 and u_2 in the *Kepler* bandpass from theoretical tables (Claret & Bloemen 2011) and employ the transit model of Mandel & Agol (2002) for our fits. We derived the transit-timing variations directly from our MCMC fit for all TRAPPIST-1 planets. We report the median and 1-sigma credible intervals of the posterior distribution functions for the 124 K2 transit timings in Tables A.1 to A.10. The resulting K2 short-cadence stacked light curves are shown on Figure 1.

3. Methodology

3.1. Dynamical modelling

Dynamical studies of the TRAPPIST-1 system are challenging due to the 7-planet, Laplace resonance-chain architecture with tight pair period ratios of 8:5, 5:3, 3:2, 3:2, 4:3 and 3:2. This configuration requires computationally-expensive orbital integrations over a large parameter space. The observed transit times are distributed over more than 550 days, corresponding to over 370 orbits of the innermost planet b. In order to accommodate the order of one billion time steps needed in a Markov Chain Monte Carlo (MCMC) method to match the timing precisions with the timespan of observations, we used graphics processing units (GPUs) and the GPU N-body code GENGA (Grimm & Stadel 2014). We calculated the orbits of all seven planets and determine the transit timing variations (TTVs) through MCMC techniques. GENGA uses a hybrid symplectic integration scheme (Chambers 1999) to run many instances of planetary systems in parallel on the same GPU. We have extended the GENGA code by implementing a GPU version of the parallel Differential Evolution MCMC (DEMCMC) technique (Braak 2006; Vrugt et al. 2009). DEMCMC deploys multiple Markov chains simultaneously that efficiently sample the highly-correlated multi-dimensional parameter space that is typical of TTV inversion problems (Mills et al. 2016). In addition we have modified the DEMCMC sampling method, such that it works more efficiently with the large correlations impacting the masses, semi-major axes and mean anomalies of the different planets.

3.2. Transit timing calculations

Following (Fabrycky 2010), we defined the X-Y plane as the plane of the sky, while planets transit in front of the star at positive values of the Z co-ordinate. The mid-transit times are found by minimising the value of the function

$$g(x_i, \dot{x}_i, y_i, \dot{y}_i) \doteq x_i \dot{x}_i + y_i \dot{y}_i, \tag{4}$$

which can be solved by setting the next time step of our numerical integrator to

$$\delta t = -g \left(\frac{\partial g}{\partial t} \right)^{-1}, \tag{5}$$

with

$$\frac{\partial g}{\partial t} = \dot{x}_i^2 + x_i \ddot{x}_i + \dot{y}_i^2 + y_i \ddot{y}_i. \tag{6}$$

The quantities x_i and y_i are the astrocentric co-ordinates of the planet i.

We used a pre-checker in the integrator to determine if a transit is expected to happen during the next time step. This will happen if the value of g_i moves from a negative value to a positive value during the next time step, and if $z_i > 0$. In addition, we used the conditions $|g/\dot{g}| < 3.5 \cdot dt$ and $r_{sky} < (R_{star} + R_i) + |v_i| \cdot dt$ to refine the pre-checker, where $|r_{sky}| = |(x_i, y_i)|$ is the radial co-ordinate on the sky plane, $|v_i|$ is the norm of the velocity, and R_i the radius of planet i; and $R_\star$ the radius of the star.

Since the integration is performed with a symplectic integrator, the co-ordinates of the position and velocity of a planet are not simultaneously known, which leads to a small error in the calculation of g. If a transit occurs very close to a time step, then it can happen that the transit is reported in both successive time

steps with a slightly different mid-transit time. But when the time step is small enough, this error can be safely neglected. Also, in highly eccentric orbits, the described pre-checker may not work properly, because *g* changes too quickly between each time step. We thus restricted ourselves in this work to eccentricities smaller that 0.2 and used the fourth-order integrator scheme with a time step of 0.08 days. When the pre-checker has detected a transit candidate, then all planets are integrated with a Bulirsh-Stoer direct N-body method for a time step and the Eq. 5 is iterated until δt is smaller than a tolerance value. A transit is reported if $r_{sky} < R_{star} + R_i$.

3.3. Orbital parameter search

To determine the best orbital parameters, we used a parallel differential evolution Markov Chain Monte Carlo method (DEM-CMC) (Braak 2006; Vrugt et al. 2009). We used *N* parallel Markov chains, where each chain consists of a *d* dimensional parameter vector $\mathbf{x}_i$. To update the population of *N* chains, each $\mathbf{x}$ is updated by generating a proposal

$$\mathbf{x}_p = \mathbf{x}_i + \gamma(\mathbf{x}_j - \mathbf{x}_k) + \mathbf{e}, \qquad (7)$$

with $i \neq j$, $i \neq k$, $j \neq k$, $\gamma = \frac{2.38}{\sqrt{2d}}$ and a small perturbation $\mathbf{e}$. The proposal is accepted with a probability $p = \min(1, \pi(\mathbf{x}_p)/\pi(\mathbf{x}_i))$. When the proposal is accepted, then $\mathbf{x}_i$ is replaced by $\mathbf{x}_p$ in the next generation; otherwise the state remains unchanged. In each 30th generation, we set $\gamma = 0.98$ to allow jumps between multimodal solutions (Braak 2006). In addition, we set $\gamma = 0.01$ and $\mathbf{x}_i = \mathbf{x}_{l \neq i}$ during the burn-in phase to eliminate outliers. Alternatively, we also tested the affine invariant ensemble walker MCMC method (Goodman & Weare 2010; Foreman-Mackey et al. 2013), which yields a comparable performance.

For the probability density function, $\pi(\mathbf{x}_i)$ we used

$$\pi(\mathbf{x}_i) = \exp\left(\frac{-\chi^2(\mathbf{x}_i)}{2})\right) = \exp\left(\frac{1}{2} - \sum_t \left(\frac{T_{calc,t} - T_{obs,t}}{\sigma_t}\right)^2\right), \qquad (8)$$

where the running index *t* refers to the transit epoch, T_{calc} are the calculated mid transit times, T_{obs} are the observed mid-transit times and σ are the observation uncertainties. Using Eq. 8, we rewrite the acceptance probability as

$$p = \min\left[1, \exp\left(\frac{-\chi^2(\mathbf{x}_p) + \chi^2(\mathbf{x}_i)}{2\tau}\right)\right], \qquad (9)$$

where τ is the MCMC sampling 'temperature'. In this work, we used values for τ between 1000 and 1. Using a large value for τ increases the acceptance probability of the next DEMCMC step and allows the walkers to explore more easily a large parameter space, but the obtained probability distribution does not correspond to the likelihood. Resampling the so-obtained likelihood region with a smaller value of τ, and starting from the median values of the previous runs, refines the sampling more accurately. Using different values of τ in an iterative order allows us to sample a large parameter space, with good accuracy in the most likely region. The median and the standard deviation are calculated with a value of $\tau = 1$. Figure 4 shows the obtained posterior probability distribution of the masses and eccentricities. We note that using a value for $\tau < 1$ in Eq. 9 would lead to smaller standard deviations.

According to (Goździewski et al. 2016), we used the following fitting parameters for the orbital elements:

$$P_i = 2\pi \sqrt{\frac{a_i^3}{G(M_\star + \tilde{m}_i)}} \qquad (10)$$

$$T_i = t + \frac{P_i}{2\pi}\left(M_i^T - M_i\right) \qquad (11)$$

$$x_i = \sqrt{e_i} \cos \omega_i \qquad (12)$$

$$y_i = \sqrt{e_i} \sin \omega_i \qquad (13)$$

$$\tilde{m}_i, \qquad (14)$$

with the period P_i, the time of the first transit T_i, the start time of the simulation *t*, the mean anomaly at the first transit M_i^T, the mean anomaly M_i, the eccentricity e_i, the argument of perihelion ω_i and the Jacobi mass $\tilde{m}_i$ for each planet *i*. The Jacobi mass of planet *i* includes also the masses of all objects with a smaller semi-major axis. We used the square root of the eccentricity in the parameters x_i and y_i to favour low eccentricity solutions. We set the longitude of the ascending node Ω_i to zero and the inclination of all planets to $\pi/2$, which allows us to calculate M_i^T through the true anomaly at the transit $\nu_i^T = \pi/2 - \omega_i$ [1].

Assuming coplanarity is motivated by the fact that the standard deviation of the derived inclinations for all seven planets with respect to the sky plane is 0.08 degrees only (Gillon et al. 2017). If the longitudes of nodes were distributed randomly on the sky, then the probability that all planets transit would be very small (most observers would see only one planet transit if this were the case). Thus, the three-dimensional mutual inclination can be constrained by simulating the angular momentum vectors of the planets drawn from an 3-D Gaussian inclination distribution of width σ_θ, allowing the density of the star to vary, ρ_*, and determining which set of parameters matches the transit durations most precisely from observers drawn from random locations on the sphere. This yields a constraint on the three dimensional inclination distributions of $\sigma_\theta < 0.3°$ at the 90% confidence level (Luger et al. 2017). Transit timing variations depend very weakly on the mutual inclinations of the planets (Nesvorný & Vokrouhlický 2014), and since these planets are constrained to be coplanar to a high degree based upon the argument in Luger et al. (2017), our model is justified in neglecting mutual inclinations of the planets for our dynamical analysis.

As initial conditions of the DEMCMC parameter search, we have randomly distributed the parameters in the range $m_i \in [0, 6 \times 10^{-6} M_\odot]$, $e_i \in [0, 0.05]$[2], $\omega_i \in [0, 2\pi]$ and $M_i \in [0, 2\pi]$. We did not assume any priors on the parameters, but restrict the eccentricity to $e < 0.2$.

A difficulty in sampling the orbital parameters of TTVs is, that there can exist strong correlations between some of the parameters, especially between *m* and *a* or between *e* and ω. The correlation between *m* and *a* can be explained, because the period P_i in Eq. 10 depends on all the masses of the more inner planets. The correlation between *e* and ω is caused by the resonance configuration, and a change in one of these parameters must be compensated by the others to get a similar time of closest approach between the planets. When the different walkers

---

[1] This equation is only valid for $i = 90°$. A discussion for the case $i \neq 90°$ is given in Gimenez & Garcia-Pelayo (1983)

[2] Tests show that setting higher initial values of *e*, up to 0.2, does not change the results. Additionally, having higher eccentricities make such a packed planetary system very likely to be dynamically unstable. In the long term stability analysis in section 6.2, the eccentricities remain below 0.025.

of the DEMCMC method are spread out over a large region in the parameter space, then the acceptance ratio of the DEMCMC steps will get very low, due to inaccurate guesses of the semi-major axes and mean anomalies.

3.3.1. Sub-step optimisation

The DEMCMC algorithm generates proposal values of the parameters, by linearly interpolating between two accepted values, but often the parameters in the optimisation problem show a non-linear dependency. This means that the DEMCMC approach always deviates from an optimal choice of the new proposal steps. Since the value of χ^2 is very sensitive to small perturbations of the semi-major axis and the mean anomaly, inaccurate guesses on these parameters will lead to dramatic high values of χ^2, and the proposal step is very unlikely to be accepted. The consequence is an acceptance ratio going towards zero as the parameters begin to populate a broader region in the parameter space. To improve this issue, we introduced a sub-step optimisation scheme to find the optimal values for the semi-major axis a and the mean anomaly M. The sub-step scheme is applied after each DEMCMC step, and has to be performed for each planet in a serial way. When the value of a or M is changed for only a single planet, then the χ^2 shows a parabolic behaviour, which enables the use of a quadratic estimator to find its optimal values x, based on three guesses x_1, x_2 and x_3 as follows:

$$x = \frac{x_1 + x_2}{2} - \frac{b_1}{2b_2},$$ (15)

with

$$b_0 = y_1$$

$$b_1 = \frac{y_2 - y_1}{x_2 - x_1}$$

$$b_2 = \frac{1}{x_3 - x_2} \cdot \left[\frac{y_3 - y_1}{x_3 - x_1} - b_1 \right],$$

where x means either a or M, and y_j means the values of χ^2 at locations x_j. The cost of the described sub-step optimisation scheme is, that three times as many walkers are needed to generate the values y_1, y_2 and y_3, and each DEMCMC step has to be followed by 14 sub-steps of computing the TTVs to adjust a and M for each planet. But even if this scheme is expensive to compute, it allows us to achieve an acceptance rate that remains $> 20 - 30\%$ for a much larger number of DEMCMC steps. The best χ^2 obtained is 342, details are listed in Table 1. The evolution of the masses and the autocorrelation functions of 5000 DEMCMC steps with the described sub-step sampling for 100 chains are shown in Figure 5, which shows efficient convergence of the chains.

3.3.2. Independent analysis

We also carried out an independent transit timing analysis with a new version of TTVFast (Deck et al. 2014) which utilises a new symplectic integrator based upon a fast Kepler solver (Wisdom & Hernandez 2015; Hernandez & Bertschinger 2015). The integrator uses a time step of 0.05 days, assumes a plane-parallel geometry, and alternates between drifts and universal Kepler steps between pairs of planets. A drift in Cartesian co-ordinates is defined as an update of some or all positions assuming constant velocities. The initial conditions are constructed with Jacobi coordinates, and the integration uses Cartesian co-ordinates in a

planet	$N_{observations}$	N_{dof}	χ^2	reduced χ^2
b	107	102	126.15	1.23
c	72	67	101.47	1.51
d	35	30	31.48	1.04
e	28	23	24.44	1.06
f	19	14	32.75	2.33
g	16	11	21.16	1.92
h	7	2	4.81	2.40
all	284	249	342.29	1.37

Table 1. Number of observations, number of degrees of freedom $N_{dof} = N_{observations} - N_{parameters}$, χ^2 from Eq. 8 and reduced $\chi^2 = \chi^2/N_{dof}$, for all planets separately and for all planets together.

center-of-mass frame. The transit times are found by tracking the projected sky position and velocity, and finding when the dot product changes sign, using Eq. 4-6. The transit centre is found by bracketing and interpolating the time steps (Deck et al. 2014). This yields timing precisions of better than a few seconds, which is sufficient to model the data given the observational uncertainties. We modelled the transit times with this code, and obtained identical masses for the maximum likelihood (within the uncertainties) , as well as broadly consistent eccentricities. Since this analysis was carried out with a different code in a different language (Julia) with a different integration technique, the fact that a similar maximum a posteriori likelihood gives confidence that we have found a unique solution for the mass ratios of this planet system.

4. Results

The TTV values of 1000 MCMC posterior samples with $\tau = 1$ are shown in Figure 2, in comparison to the observed transit times. The TTV residuals for each transit are shown in Figure 3. We compute the planet densities ρ_p independently from the stellar mass, by using the planetary radii- and mass-ratio posteriors $\frac{M_p}{M_\star}$ and $\frac{R_p}{R_\star}$, along with the well constrained stellar density $\rho_\star$ determined photometrically from the *Spitzer* dataset (Seager & Mallén-Ornelas 2003). The planet density then is $\rho_p = \rho_\star \frac{M_p}{M_\star} \frac{R_\star^3}{R_p^3}$ (Jontof-Hutter et al. 2014). Using the stellar density from the photometry is valid in our case because the planets' eccentricities are found to be small. Determining planetary densities using this approach effectively removes any inaccuracy from the stellar models and improves our constraints on the planetary interiors. To transform our results into physical masses and radii, we use the most recent stellar mass estimate of $0.089 \pm 0.007\ M_\odot$ (Van Grootel et al. 2018).

Our resulting posterior distribution functions for the masses and eccentricities for all seven planets are shown in Figure 4. To perform the search over a large parameter space, different sampling 'temperatures' τ are used in an iterated order. Through our extensive exploration of the parameter space we find that the masses and eccentricities for all planets are reasonably constrained (3% - 9% for mass, and 6% - 25% for eccentricity). Table 2 summarises the planetary physical parameters (mass and radius ratios) while Table 3 displays the planets' orbital parameters. A full posterior distribution between all mutual pairs of parameters is shown in Figure 6.
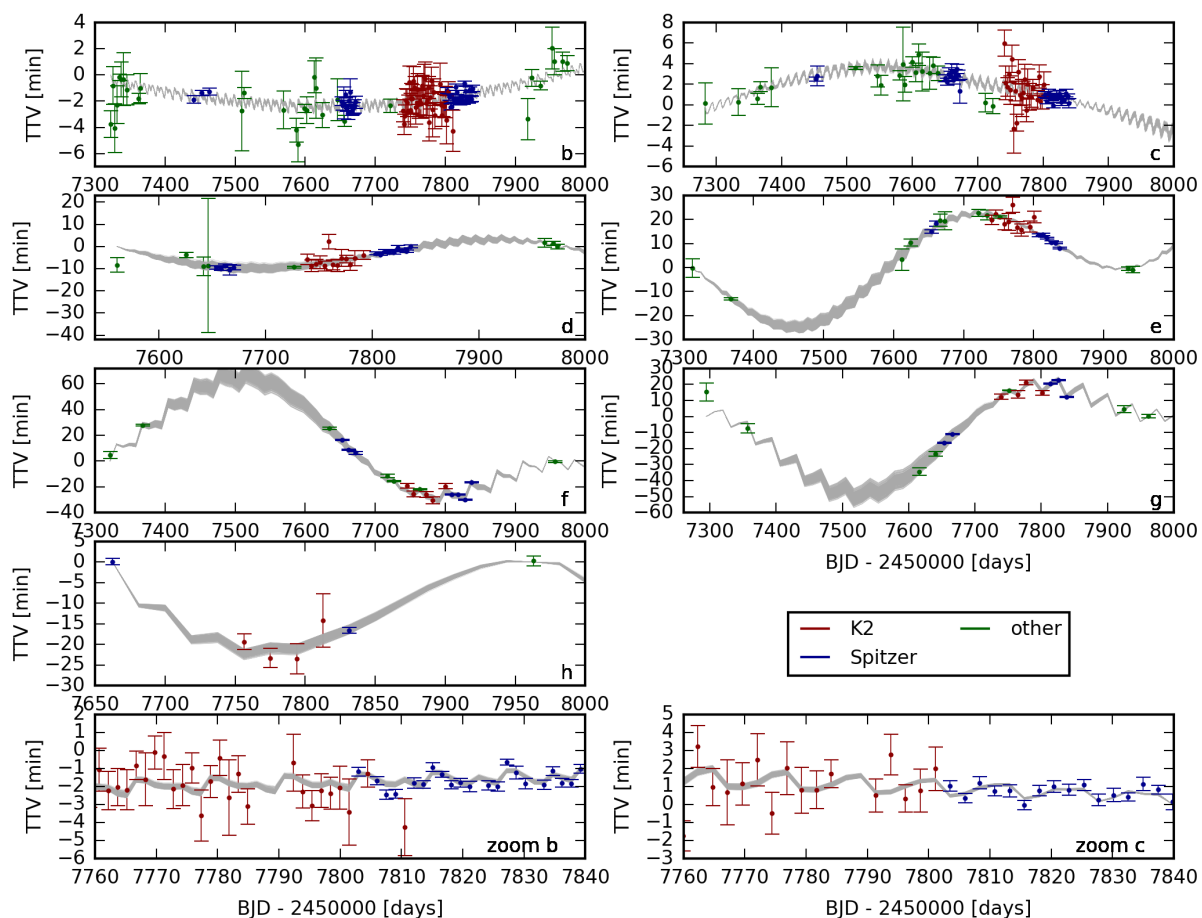
Fig. 2. Calculated TTVs for all planets and for 1000 different MCMC samples (grey lines). Measured transit times with the corresponding uncertainties are indicated by coloured symbols, according to the used telescope. A detailed list of all transits is given in the appendix. The differences between the solutions reflect the distribution shown in Figure 4 for $\tau = 1$. The two panels at the bottom show a zoomed region for planet b and c.

planet	m [$M_\oplus$]	$-\sigma$	$+\sigma$	R [$R_\oplus$]	$-\sigma$	$+\sigma$	$c_{m,r}$	ρ [$\rho_\oplus$]	$-\sigma$	$+\sigma$	Surf. grav.[g]	$-\sigma$	$+\sigma$
b	1.017	0.143	0.154	1.121	0.032	0.031	0.502	0.726	0.091	0.092	0.812	0.102	0.104
c	1.156	0.131	0.142	1.095	0.031	0.030	0.624	0.883	0.078	0.083	0.966	0.087	0.092
d	0.297	0.035	0.039	0.784	0.023	0.023	0.569	0.616	0.062	0.067	0.483	0.048	0.052
e	0.772	0.075	0.079	0.910	0.027	0.026	0.708	1.024	0.070	0.076	0.930	0.063	0.068
f	0.934	0.078	0.080	1.046	0.030	0.029	0.855	0.816	0.036	0.038	0.853	0.039	0.040
g	1.148	0.095	0.098	1.148	0.033	0.032	0.863	0.759	0.033	0.034	0.871	0.039	0.040
h	0.331	0.049	0.056	0.773	0.027	0.026	0.386	0.719	0.102	0.117	0.555	0.076	0.088

Table 2. Updated masses, radii (Delrez et al. 2018), correlation coefficients $c_{m,r}$ of masses and radii as well as the densities and the surface gravity of all seven planets.

5. Comparison with other studies

At the time of writing, we are aware of a preprint by Wang et al. (2017) that re-analysed our initial Spitzer and ground-based datasets, and added in K2 transit timing measurements. Wang et al. (2017) utilises TTVFast (Deck et al. 2014), which also employs a symplectic integrator. Our analysis improves upon their initial analysis in several ways:

1. We account for the correlations in mass and radius when computing the constraints on the planets in the mass-radius

plane. The density is better constrained than either the mass or radius, leading to a strong correlation between planetary mass and radius (Figure 10), which parallels the isocomposition contours, and so our approach should improve the constraint upon composition.

2. We utilise a new set of Spitzer transit times, which, compared with the K2 times, are superior in timing precision by about a factor of two, cover a longer time duration (> 100 days), and are less affected by stellar variability.

3. Our fast, parallel GPU integration scheme coupled with a parallel MCMC algorithm allows a thorough exploration of
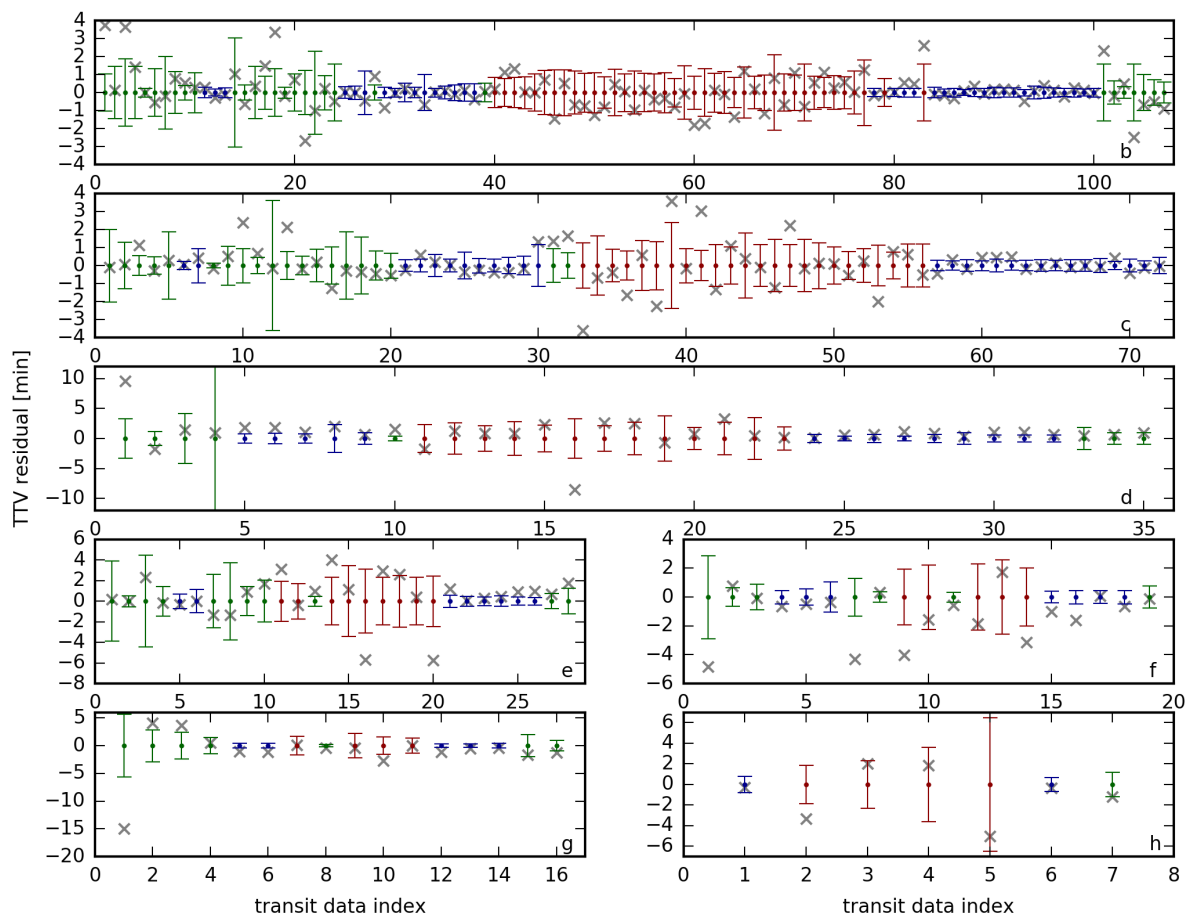
Fig. 3. Residuals of the TTVs shown in Figure 2. The transit data index corresponds to the column index of the tables A.1 - A.10 .

planet	a [au]	σ_a	e	σ_e	ω [°]	σ_ω	M [°]	σ_M
b	0.01154775	5.7e-08	0.00622	0.00304	336.86	34.24	203.12	34.34
c	0.01581512	1.5e-07	0.00654	0.00188	282.45	17.10	69.86	17.30
d	0.02228038	4.4e-07	0.00837	0.00093	-8.73	6.17	173.92	6.17
e	0.02928285	3.4e-07	0.00510	0.00058	108.37	8.47	347.95	8.39
f	0.03853361	4.8e-07	0.01007	0.00068	368.81	3.11	113.61	3.13
g	0.04687692	3.2e-07	0.00208	0.00058	191.34	13.83	265.08	13.82
h	0.06193488	8.0e-07	0.00567	0.00121	338.92	9.66	269.72	9.51

Table 3. Median and standard deviation σ of the semi-major axis a, eccentricity e, argument of periapsis ω, and mean anomaly M of the seven planets. These results are obtained from the MCMC runs with $\tau = 1$, using a fixed stellar mass of 0.09 $M_\odot$.

parameter space. The reduced chi-square of our best fits are near unity, while Wang et al. (2017) utilise models with high reduced chi-square in their analysis.

These improvements over the Wang et al. (2017) analysis should lead to more robust and accurate constraints upon the compositions, masses and radii of the planets.

6. Dynamical properties of the TRAPPIST-1 system

In this section we use the results of our dynamical modelling of the system to investigate the degeneracies in the planetary parameters and the stability of the system over long time-scales.

6.1. Tackling degeneracies

Degeneracies commonly plague TTV inversion problems (Agol & Fabrycky 2017), in particular, between mass and eccentricity (Lithwick et al. 2012). However, Figure 4 shows that the eccentricities and masses are well constrained for all seven TRAPPIST-1 planets. A combination of the 1) high-precision *Spitzer* photometry, 2) *K2*'s 80-day long quasi-continuous coverage and the 3) resolved high-frequency component of the TTV pattern known as 'chopping'(Holman et al. 2010; Deck & Agol 2015) all contribute to mitigate the mass-eccentricity degeneracy. The chopping patterns for all planets except for h are detected in the data (Figure 2), while their periodicities encode the
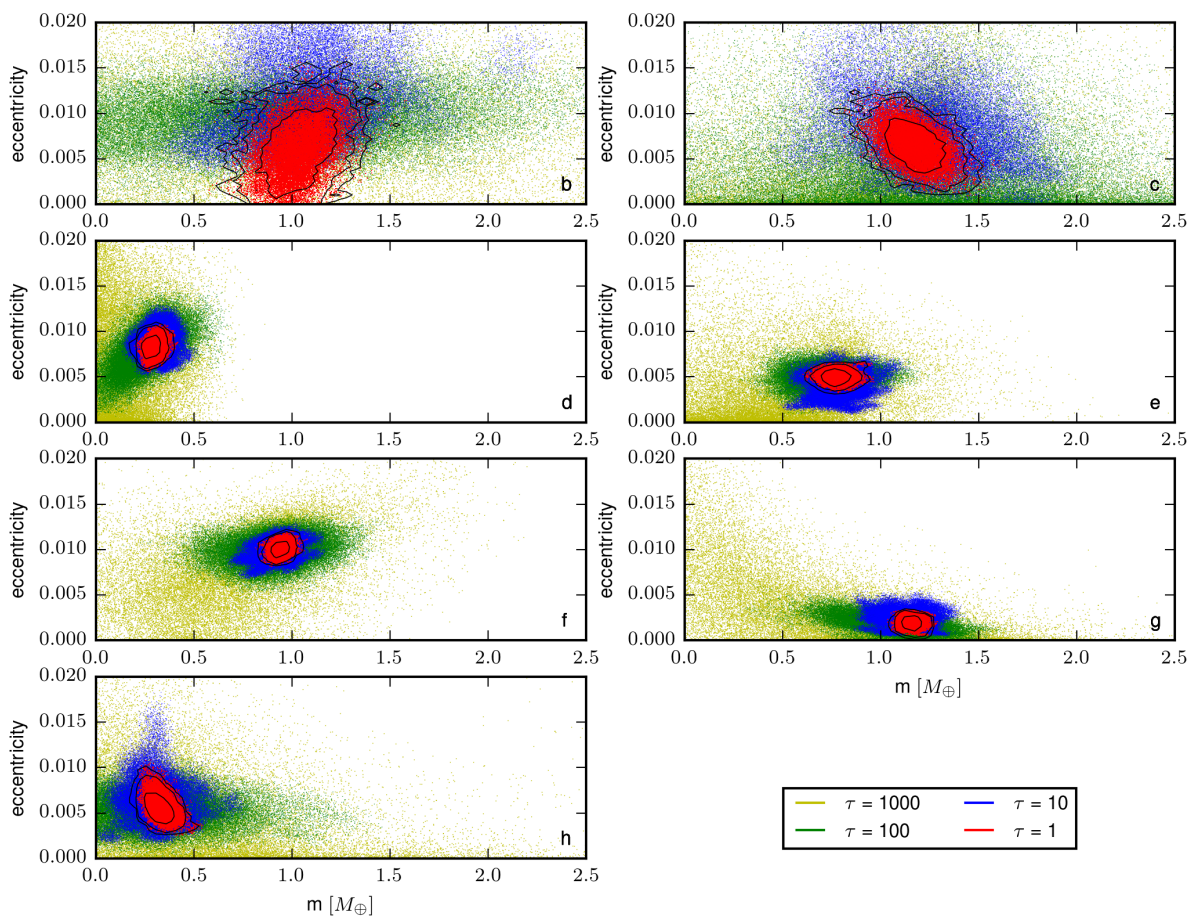
Fig. 4. Posterior probability distribution of the mass and eccentricities of all seven planets, for different MCMC sampling 'temperatures' τ, assuming a stellar mass of $M_\star = 0.09 M_\odot$ (Van Grootel et al. 2018). The contours correspond to significance levels of 68%, 95% and 99% for $\tau = 1$. Sampling 'temperatures' greater than one are used to cover a larger parameter space.

timespan between successive conjunctions of pairs of successive planets whose amplitudes yield the masses of adjacent perturbing planets.

6.2. Long-term stability

We study in the following the temporal evolution of the eccentricities and arguments of periapsis, respectively, for all seven planets over 10 Myr. The discussion on the evolution of the argument of periapsis and eccentricities for all planets are based on Figures 7 and 8. We show on Figure 9 the temporal evolution of the Laplace three body resonant angles ϕ. Eccentricities remain below 0.025 for all planets and show a very regular evolution for 2 Myr (i.e. 487 millions orbits of planet b and close to 30 millions of planet h). After that, the eccentricities evolve more irregularly, but are still bound to low values. The arguments of periapsis, however, exhibit different behaviours. All planets show an average precession of $\dot\omega \approx 2\,\pi/\,300$ years. Planets d, e, f, and g show a more sporadic evolution, with ω undergoing periodic phases of fast precession during which $\dot\omega > 2\pi/\text{year}$. This behaviour arises from the small eccentricities and strong mutual gravitational perturbations between the planets. We also study the evolution with time of the three-body Laplace angles

ϕ. The initial values of ϕ agree well with reported values(Luger et al. 2017) but after 2 Myr, the resonance chain is perturbed. This behaviour reflects well the evolution of the eccentricities and is an indication that the initial conditions we are using are not known sufficiently accurately to assess resonances over very-long timescales. The exact solution should survive for several Gyrs in the resonance chain as the TRAPPIST system is comprised of a suite of resonance chains (Luger et al. 2017).

Tides could in addition be particularly important in this closely-packed system (Luger et al. 2017). Tides damp eccentricity and stabilise the dynamical perturbations. Preliminary results using the Mercury-T code (Bolmont et al. 2015) show that a small tidal dissipation factor at the level 1% that of the Earth (Neron de Surgy & Laskar 1997) would generate a tidal heat flux of 10-20 W/m^2, which is significantly higher than Io's tidal heat flux(Spencer et al. 2000) of 3 W/m^2. Given the estimated age of the system, most of the eccentricity of planet b at least should have been damped.

7. The nature of the TRAPPIST-1 planets

Our improved masses and densities show that TRAPPIST-1 c and e likely have largely rocky interiors, while planets b, d, f,
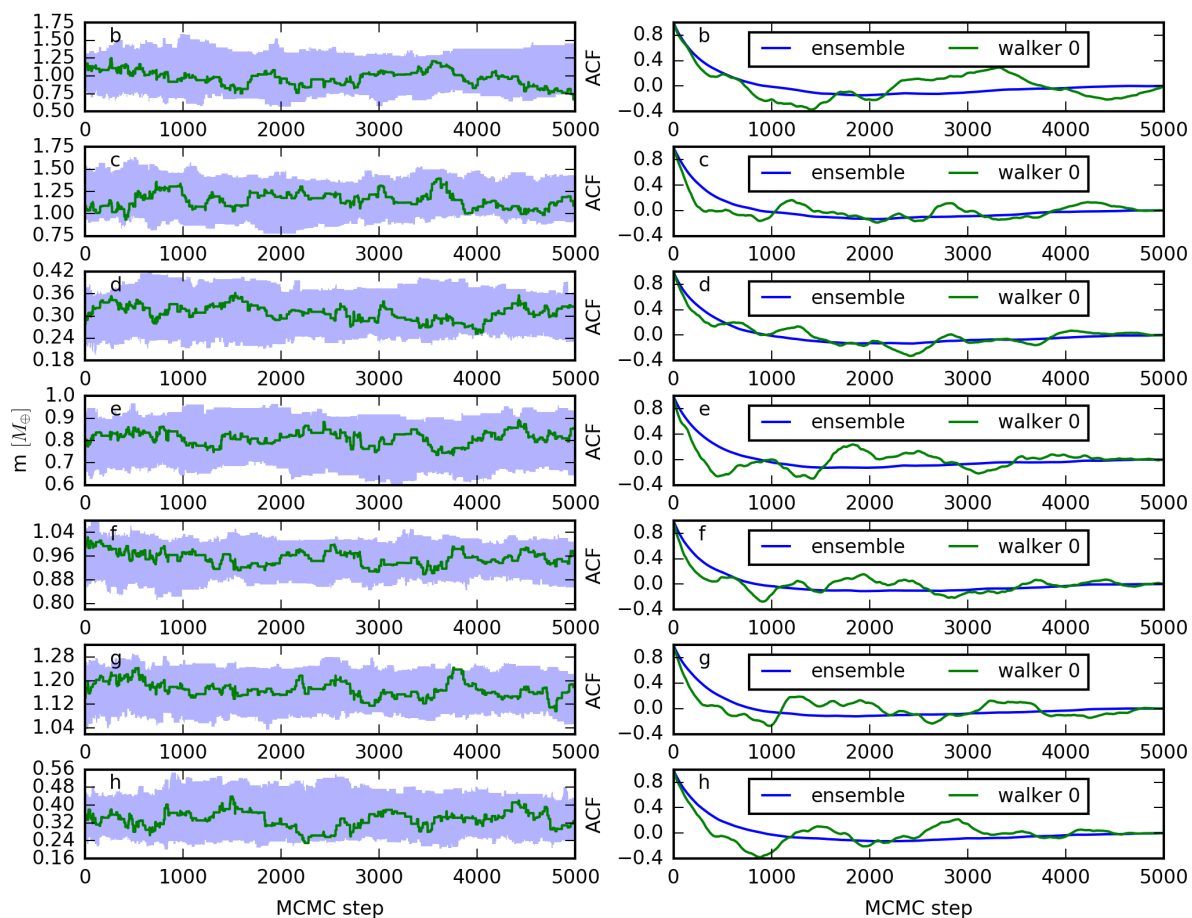
Fig. 5. Left panels: evolution of the masses of all planets of the entire ensemble of 100 walker chains in blue, and the evolution of a single chain in green. Right panels: the auto-correlation function of the masses for the ensemble and a single chain.

g, and h require envelopes of volatiles in the form of thick atmospheres, oceans, or ice, in most cases with water mass fractions ≲ 5% (Figure 10). These values are close to the ones inferred by another recent study based on mass-radius modelling (Unterborn et al. 2017). It is also consistent with accretion from embryos that grew past the snow line and migrated inwards through a region of rocky planet growth.

7.1. Planetary interiors

We calculate the theoretical mass-radius curves shown in Figure 10 for interior layers of rock, ice, and water ocean following the thermodynamic model of Dorn et al. (2017). This model uses the equation of state (EoS) model for iron by Bouchet et al. (2013). The silicate-mantle model of Connolly (2009) is used to compute equilibrium mineralogy and density profiles for a given bulk mantle composition. For the water layers, we follow Vazan et al. (2013), using a quotidian equation of state (QEOS) for low pressure conditions and the tabulated EoS from Seager et al. (2007) for pressures above 44.3 GPa. We assume an adiabatic temperature profile within core, mantle and water layers.

The mass-radius diagram in Figure 10 compares the TRAPPIST-1 planets with theoretical mass-radius relations calculated with published models (Dorn et al. 2017). We estimate

the probability $p_{\text{volatiles}}$ of each planet to be volatile-rich by comparing masses and radii to the idealised composition of Fe/Mg = 0 and Mg/Si = 1.02 (Figure 10), which represents a lower bound on bulk density for a purely rocky planet. Planets b, d, f, g, and h very likely contain volatile-rich layers (with $p_{\text{volatiles}}$ of at least 0.96, 0.99, 0.66, 1, and 0.71, respectively). Volatile-rich layers could comprise atmosphere, oceans, and/or ice layers. In contrast, planets c and e may be rocky (with $p_{\text{volatiles}}$ of at least 0.24 and <0.01, respectively).

The comparison of masses and radii with the idealised interior end-member of $m_{\text{water}}/M = 0.05$ (fixed surface temperature of 200 K, Figure 10, blue solid line) suggest that all planets, except planet b and d, do very likely not contain more than 5% mass fraction in condensed water. For planets b and d, we thereby estimate a probability of 0.7 and 0.5 to contain less than 5 % water mass fraction. However, because the runaway greenhouse limit for tidally locked planets lies near the orbit of planet d (Kopparapu et al. 2016; Turbet et al. 2017), the large amount of volatiles needed to explain the radius of the most irradiated planet b is likely to reside in the atmosphere (possibly as a supercritical fluid), reducing the mass fraction needed in a condensed phase.
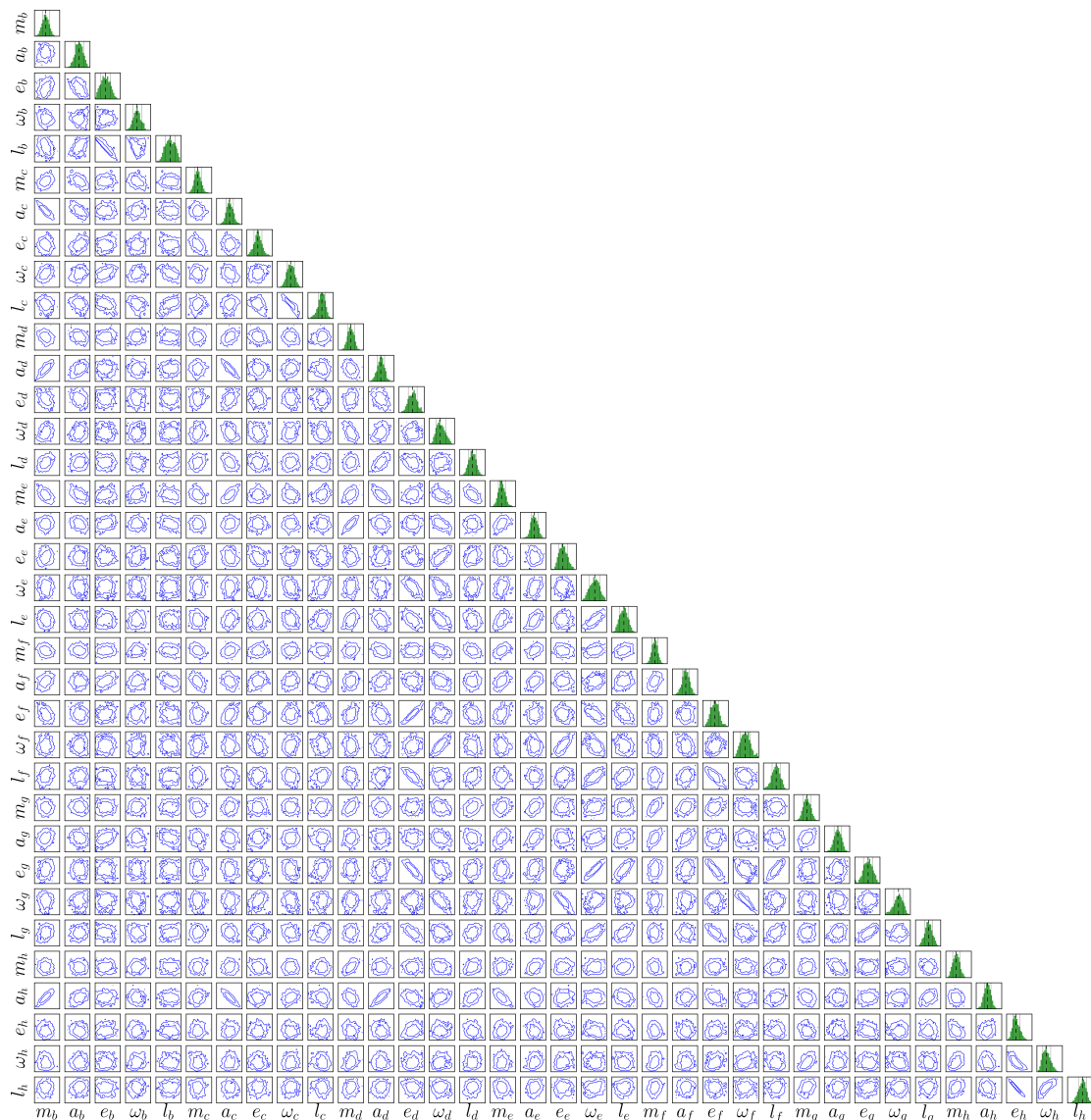
Fig. 6. Posterior probability distribution between all pairs of parameters, the masses m, the semi-major axes a, the eccentricities e, the arguments of perihelion ω, and the mean longitudes $l = \Omega + \omega + M$ of all seven planets. It is showing strong correlations between many pairs of parameters, especially between m and a and between e and ω.

7.2. Limits for the possible atmosphere-scenarios

We use the LMD-G one-dimensional cloud-free numerical climate model (Wordsworth et al. 2010) to simulate the vertical temperature profiles of the seven TRAPPIST-1 planets. Calculations are performed using a synthetic spectrum of TRAPPIST-1 and molecular spectroscopic properties from Turbet et al. (2017). We assume atmospheric compositions that range from pure H_2, H_2-CH_4, H_2-H_2O to pure CO_2. We further assume a volume molecular mixing ratio of 5×10^{-4} for methane and 1×10^{-3} for water, to match solar abundances in C and O(Asplund et al.

2009). We finally assume a core composition of Fe/Mg = 0.75 and Mg/Si= 1.02 (Unterborn et al. 2017).

For each planet, atmospheric composition and a wide range of surface pressures (from 10 mbar to 10^3 bar, see Table 4), we decompose the thermal structure of the atmosphere into 500 log-spaced layers in altitude co-ordinates. We estimate the transit radii of the planets, as measured by *Spitzer* in the 4.5μm IRAC band, solving radiative transfer equations including molecular absorption, Rayleigh scattering, and various other sources of continuua, that are Collision Induced Absorptions (CIA) and/or far line wing broadening, when needed and available. Radiative
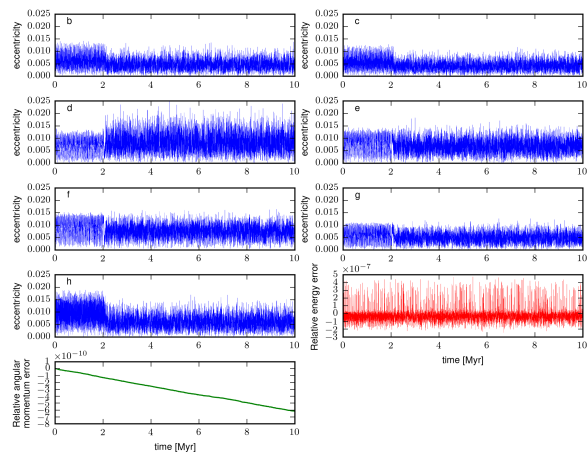
Fig. 7. Temporal evolution of the eccentricities of all planets. The eccentricities are well constrained to values below 0.015 and show a regular behaviour for 2 Myr. After that, the systems shows irregularities, caused by small uncertainties in the initial conditions. We also show the relative energy error and the relative angular momentum error of the integrator.
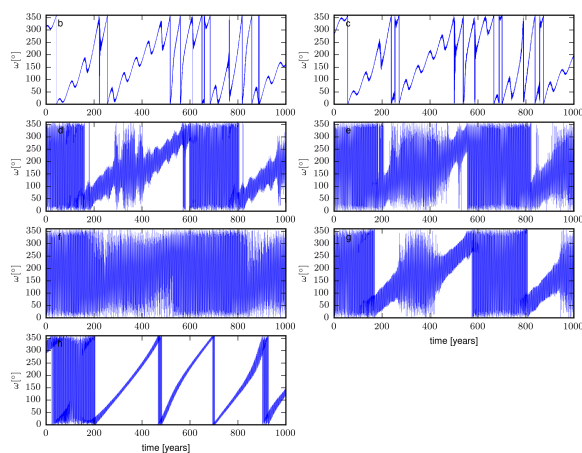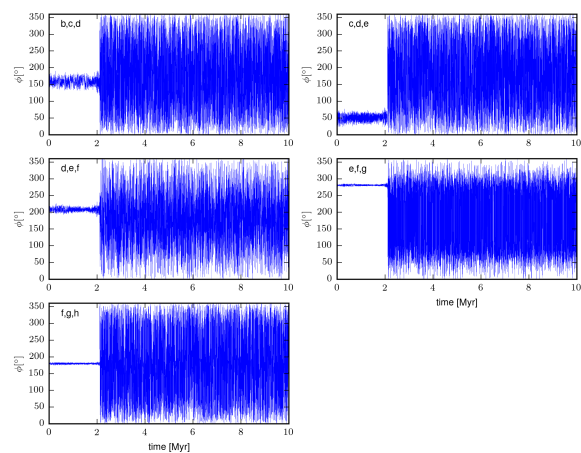

Fig. 9. Temporal evolution of the three body resonant angle $\phi_i = p\lambda_{i-1} - (p+q)\lambda_i + q\lambda_{i+1}$, where the values of p and q for consecutive triples of planets are (2,3), (1,2), 2,3), (1,2) and (1,1)(Luger et al. 2017). After 2 Myr, the systems shows irregularities, caused by small uncertainties in the initial conditions.

Fig. 8. Temporal evolution of ω, showing a fast precession and strong mutual orbital perturbations between the planets.

transfer equations are solved through the 500 layers in spherical geometry (Waldmann et al. 2015) to determine the effective transit radius of a given configuration in the Spitzer band.

A fit was found when the surface pressure resides at the nominal transit radius of the *Spitzer* observations and thus corresponds to the maximum surface pressure. It is maximal in the sense that any reservoir of volatiles at the surface would yield a higher core radius and reduce the mass of the atmosphere needed to match the observed radius.

For atmospheres with a higher mean molecular weight, the inferred pressures are too large for a perfect gas approximation. Assuming that the mass of the atmosphere is much lower than the core, the surface pressure $P_{\rm surf}$ can be estimated by integrating the hydrostatic equation, which yields:

$$P_{\rm surf} = P_{\rm transit}\ \exp\left(\left(1 - \frac{R_{\rm core}}{R_{\rm transit}}\right)\frac{R_{\rm core}}{H}\right),\qquad(16)$$

where $P_{\rm transit}$ is the pressure at the transit radius $R_{\rm transit}$, $R_{\rm core}$ the radius at the solid surface, $H = \frac{kT}{\mu m_H g}$ the mean atmospheric scale height, k is Boltzmann's constant, T the surface temperature, μ the mean molecular weight, and m_H the mass of the hydrogen atom. This relation demonstrates that the surface pressure increases exponentially with $\frac{\mu}{T}$; and is why, at the low temperatures expected for the planets beyond d, it is difficult to explain the observed radii with an enriched atmosphere above a bare core (with a standard Earth-like composition) without unrealistically large quantities of gas.

For the colder, low density planets (f, g, and h), explaining the radius with only a CO_2 atmosphere is difficult due to the small pressure scale height and the fact that CO_2 should inevitably collapse on the surface beyond the orbit of planet g (Turbet et al. 2017). We acknowledge that these various results could be challenged with a significantly different rock composition or thermal state of the planets.

Planet b however, is located beyond the runaway greenhouse limit for tidally locked planets (Kopparapu et al. 2016; Turbet et al. 2017) and could potentially reach – with a thick water vapour atmosphere – a surface temperature up to 2000 K (Kopparapu et al. 2013). Assuming more realistic mean temperatures of 750-1500 K, the above estimate yields pressures of water vapour of the order of 10^1-10^4 bar, which could explain its relatively low density (assuming $P_{\rm transit} = 20$ millibar). As such, TRAPPIST-1 b is the only planet above the runaway greenhouse limit which seems to require volatiles.

Given the density constraints and assuming a standard rock composition(Unterborn et al. 2017), planets b to g cannot accommodate H_2-dominated atmospheres thicker than a few bars. Within these assumptions and considering the expected intense atmospheric escape around TRAPPIST-1 (Bolmont et al. 2017), the lifetime of such atmospheres would be very limited, making this scenario rather unlikely. For heavier molecules, the surface pressure needed to match a given radius varies roughly exponentially with the mean molecular weight, which imposes enormous surface pressures for which a more detailed equation of state would be needed.
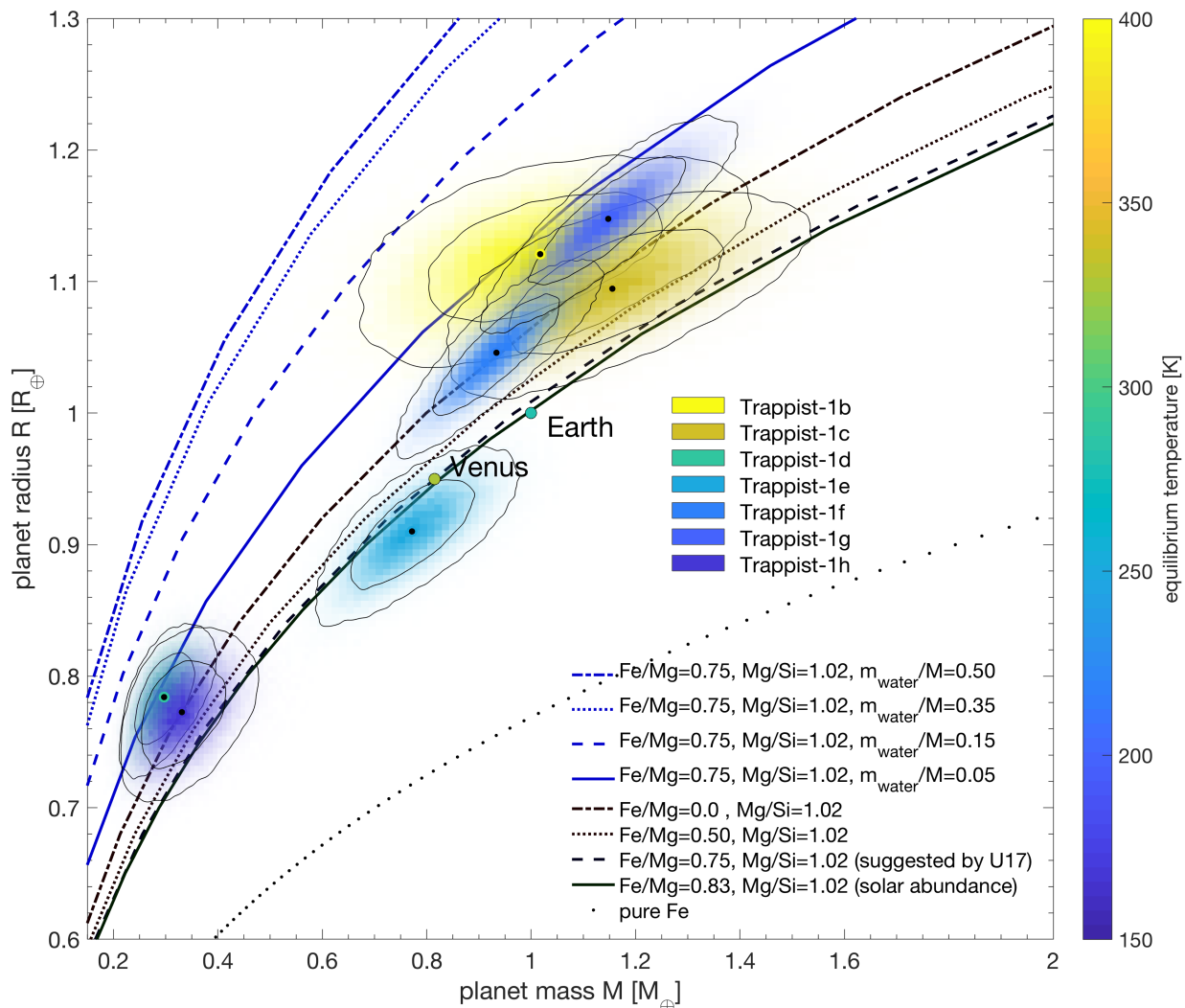
Fig. 10. Mass-radius diagram for the TRAPPIST-1 planets, Earth, and Venus. Curves trace idealised compositions of rocky and water-rich interiors (surface temperature fixed to 200 K). Median values are highlighted by a black dot. Coloured contours correspond to significance levels of 68% and 95% for each planet. The interiors are calculated with model II of Dorn et al. (2017). Rocky interiors are composed of Fe, Si, Mg, and O, assuming different bulk ratios of Fe/Mg and Mg/Si. U17 refers to Unterborn et al. (2017). Equilibrium temperatures for each planet are indicated by the coloured contours.

7.3. Mass-ratios, densities and irradiation

The mass of a celestial object is its most fundamental property. We now compare the masses of the TRAPPIST-1 planets and place them into wider context. Exoplanet discoveries are heavily biased towards single Sun-like stars. TRAPPIST-1 provides a glimpse of what results around stars, and within disks, that are one order of magnitude lighter than the norm.

Figure 11 displays a mass-ratio versus period diagram comparing the TRAPPIST-1 system to other exoplanets (where the orbital period is used to separate various sub-populations). We also push the comparison to include the planets of the Solar system, and the principal moons of Jupiter. TRAPPIST-1's planets cover mass-ratio a range $10^{-4} - 10^{-5}$, which is shared with the sub-Neptune and super-Earth exoplanets population that orbits Sun-like stars. The similarity may suggest a similar formation mechanism, or at minimum a comparable scaling in protoplane-

tary disk mass. Notably, sub-Neptunes and super-Earths are the most abundant planet types for Sun-like stars (Mayor et al. 2011; Howard et al. 2012). This region also encompasses the Galilean satellite system, and thus reflects a host or satellite configuration that spans over three orders of magnitude in mass, like has been noticed in the literature (Canup & Ward 2006).

The irradiation of the TRAPPIST-1 planets plays an important role in their evolution. It is thus also insightful to compare the TRAPPIST-1 masses and incident flux in the context of the currently known exoplanet population. Figure 12 shows a focus on planets receiving irradiation that spans Mars to Venus and 0.1 to 4.5 $M_\oplus$. The upper mass limit is set to 4.5 $M_\oplus$ because this corresponds to 1.5 $R_\oplus$, an indicative limit for rocky worlds (Rogers 2015; Fulton et al. 2017). The lower mass limit was arbitrarily set to 0.1 $M_\oplus$, corresponding to Mars, to represent objects that have difficulties retaining an atmosphere. It is interesting to note that TRAPPIST-1d & e are the only transiting exoplanets in this

Planet	M_{core}	R_{core}	$R_{transit}$	$P_{surf, H_2/CH_4}$	$P_{transit, H_2/CH_4}$	$P_{surf, H_2/H_2O}$	$P_{transit, H_2/H_2O}$
T1-b	1.02	1.01	1.12	5	0.2	5	0.2
T1-c	1.18	1.06	1.10	1	0.2	1	0.3
T1-d	0.281	0.697	0.766	2	0.3	2	0.3
T1-e	0.766	0.913	0.913	x	x	x	x
T1-f	0.926	0.986	1.05	5	0.4	cond.	cond.
T1-g	1.14	1.05	1.15	2×10^1	0.4	cond.	cond.
T1-h	0.313	0.719	0.775	2	0.4	cond.	cond.

Table 4. Planetary characteristics of the TRAPPIST-1 planets derived from our 1-D numerical climate simulations. M_{core} and R_{core} are the mass and radius of the core, with a composition assumed to be Fe/Mg = 0.75 and Mg/Si= 1.02. $R_{transit}$ are the transit radii measured by *Spitzer*. Adopted masses and radii are expressed in Earth units ($M_\oplus$ and $R_\oplus$, respectively). Surface pressures P_{surf} (i.e. the pressure at the core or atmosphere boundary) and transit pressures $P_{transit}$ (i.e. the atmospheric pressure at the transit radius) are expressed in bars. CH_4 and H_2O volume mixing ratios were arbitrarily fixed according to C/O solar abundances; that is, 5×10^{-4} and 1×10^{-3}, respectively. 'cond.' indicates those cases where water vapour (at solar abundance) starts to condense in the atmosphere, and should thus be highly depleted. We note that, given the assumptions made on the core composition, TRAPPIST-1e cannot accommodate a H_2-dominated atmosphere at all.
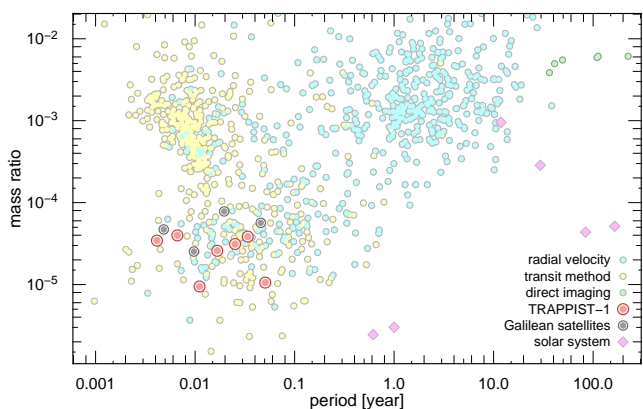

Fig. 11. Ratio between the mass of a planet or moon and that of its host as a function of orbital period. We represent the known population of exoplanets (from exoplanet.eu (Schneider et al. 2011)) from three different detection methods. The Solar system is also highlighted. The TRAPPIST-1 system, like the Galilean moons of Jupiter, share a similar parameter space with the sub-Neptune and super-Earth population. Orbital periods are used to reveal the various sub-populations.

Fig. 12. Masses, and the incident fluxes received by the TRAPPIST-1 planets, compared to other exoplanets found by the transit method (yellow), via the radial-velocity technique (blue), and to the terrestrial worlds of the Solar system (grey). We highlight two ranges of interest in mass and incident flux. All objects contained in the exoplanet.eu catalogue (Schneider et al. 2011), found by the RV, or the transit method, are included in this figure.

region. The closest other known transiting planets are LHS 1140 b (0.4, 6.65) (Dittmann et al. 2017) & Kepler-138b (0.64,2.33) (Jontof-Hutter et al. 2015), and both of these have much larger uncertainties on their densities (27% and 92% respectively).

We complete this section by comparing the density of the TRAPPIST-1 planets with their irradiation level in Figure 13. We note that the density trend vs. irradiation increases until TRAPPIST-1e, where it peaks and then decreases for the outer planets. One object stands out of that pattern, TRAPPIST-1d, which interestingly, has a similar bulk density as the Moon. These aspects will be particularly relevant to better understand the formation pathway of the TRAPPIST-1 system.

7.4. Migration and composition

The combination of a planetary system's orbital architecture and the planets' densities can constrain where the planets grew (or at least their feeding zones) as well as their orbital histories (Raymond et al. 2008).
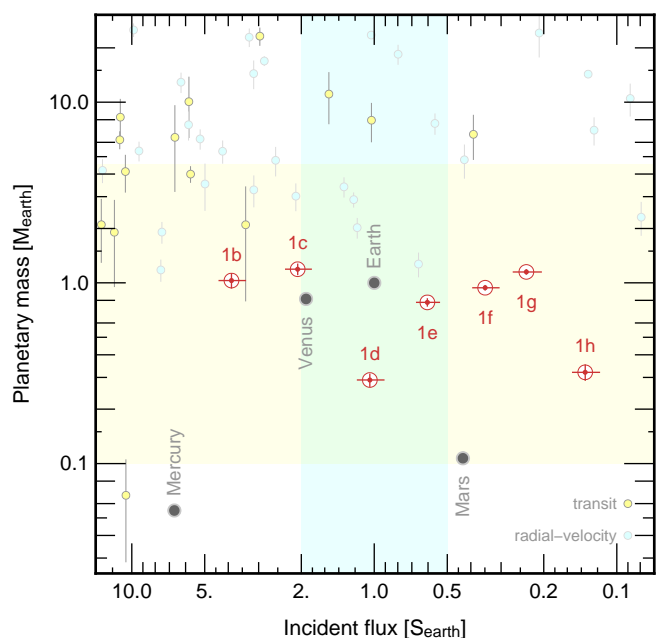
Based on cosmochemical abundances (Lodders 2003), one would expect objects that condensed past the snow line to contain a significant fraction (up to 50%) of ice. However, other effects can reduce planets' water contents, such as desiccation of constituent planetesimals by short-lived radionuclides (Grimm & McSween 1993), water loss during giant impacts between embryos (Genda & Abe 2005), and heating during the very rapid growth expected around low-mass stars (Lissauer 2007; Raymond et al. 2007). In addition, embryos do not migrate inwards through an empty expanse towards the inner parts of the disk. Rather, they likely migrate through a region in which rocky ma-
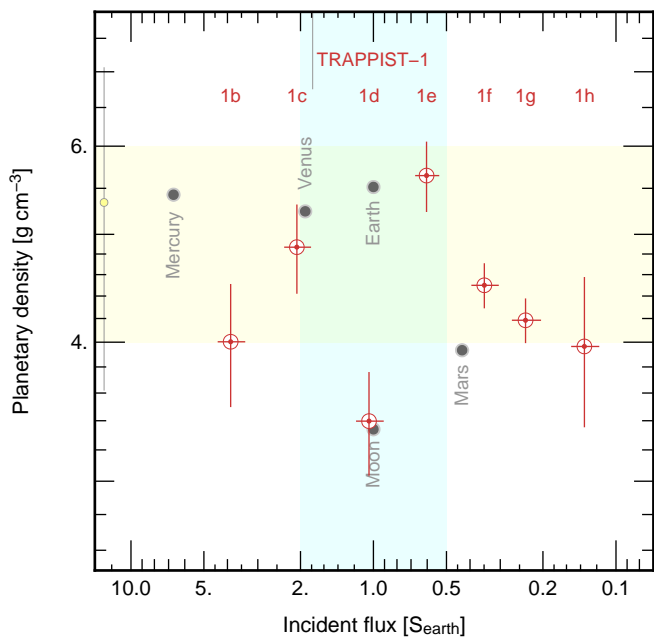
Fig. 13. Densities, and the incident fluxes received by the TRAPPIST-1 planets (red), compared to the Solar System's telluric planets and the Moon (grey). Other exoplanets with reported uncertainties on mass and radius smaller than 100% are shown in yellow and originate from the TEPCAT catalogue (Southworth 2011).

terial is already growing (Izidoro et al. 2014). The water contents of migrating icy embryos are likely to be diluted by impacts with rocky embryos. In some situations, migrating icy embryos can stimulate the growth of large rocky embryos, creating a large density contrast between neighbouring planets (Raymond et al. 2006).

Gravitational interactions with the gaseous disk cause ~Earth-mass planetary embryos to migrate, usually inwards (Ward 1997; Baruteau et al. 2014). Current models invoke two steps in the growth of these embryos. First, as dust coagulates and drifts through the disk (Güttler et al. 2010; Birnstiel et al. 2012), 10-100 km-scale planetesimals form by a hydrodynamical instability (such as the streaming instability; (Youdin & Goodman 2005; Johansen et al. 2014)) in regions where the local solids-to-gas ratio is sufficiently high (Drążkowska & Dullemond 2014; Carrera et al. 2015). These conditions are expected to be met first beyond the snow line (Armitage et al. 2016; Schoonenberg & Ormel 2017). Next, the largest planetesimals grow rapidly by accreting inwards-drifting pebbles (Ormel & Klahr 2010; Lambrechts & Johansen 2012). Models of pebble accretion find that large embryos preferentially grow beyond the snow line (Morbidelli et al. 2015; Ormel et al. 2017). However, embryos' growth is self-limiting. When an embryo reaches a critical mass, it creates a pressure bump in the gas disk exterior to its orbit, which traps drifting pebbles and shuts off pebble accretion (Lambrechts et al. 2014). This critical mass depends on the disk structure but was calculated by Ormel et al. (2017) to be $\sim 0.7 M_\oplus$ for the case of TRAPPIST-1 (for a specific disk model), close to the actual planet masses. In their model, embryos form sequentially, reaching this critical mass before migrating inwards.

The resonant structure of the TRAPPIST-1 system (Luger et al. 2017) is a telltale sign of orbital migration (Terquem & Papaloizou 2007; Ogihara & Ida 2009). The fact that all seven plan-

ets form a single resonant chain indicates that the entire system migrated in concert (Cossou et al. 2014; Izidoro et al. 2017). Indeed, orbital solutions generated by disk-driven migration have been shown to be more stable than other solutions (Tamayo et al. 2017b). Whereas most resonant systems are likely to be unstable ((Izidoro et al. 2017; Matsumoto et al. 2012)), the TRAPPIST-1 can be interpreted as a system that underwent a relatively slow migration creating a long-lived resonant system.

8. Conclusions

In this paper we have used the most recent set of transit timings of the TRAPPIST-1 system to constrain the masses, densities of the seven Earth-size planets found earlier this year. Our purpose-built TTV code enables an extensive exploration of the parameter space combined to a full n-body integration scheme. Our results yield a significant improvement in our knowledge of the planetary bulk density, with corresponding uncertainties ranging between 5 and 12%. This level of precision is unprecedented for exoplanets receiving modest irradiation in this mass range. Our conclusions regarding the nature of the TRAPPIST-1 planets are the following:

– The TRAPPIST-1 planets display densities ranging from 0.6 to 1.0 $\rho_\oplus$.
– TRAPPIST-1 c and e likely have largely rocky interiors.
– TRAPPIST-1 b, d, f, g and h require envelopes of volatiles in the form of thick atmospheres, oceans, or ice, in most cases with water mass fractions $\lesssim 5\%$. For comparison, the Earth's water content is $< 0.1\%$.
– TRAPPIST-1 d, e, f, g and h are unlikely to have an enriched atmosphere (e.g. CO_2) above a bare core (assuming a standard Earth-like composition) without invoking unrealistically large quantities of gas.
– TRAPPIST-1 b is the only planet above the runaway greenhouse limit that seems to require volatiles, with pressures of water vapour of the order of 10^1-10^4 bar.

These updated mass and density measurements represent key information for upcoming studies straddling astrophysics, planetary sciences and geophysics aimed at an improved understanding of the interiors of temperate, Earth-sized planets.

References

Agol, E. & Fabrycky, D. 2017, ArXiv e-prints [arXiv:1706.09849]

Agol, E., Steffen, J., Sari, R., & Clarkson, W. 2005, Monthly Notices of the Royal Astronomical Society, 359, 567

Aigrain, S., Hodgkin, S. T., Irwin, M. J., Lewis, J. R., & Roberts, S. J. 2015, Monthly Notices of the Royal Astronomical Society, 447, 2880

Aigrain, S., Parviainen, H., & Pope, B. J. S. 2016, Monthly Notices of the Royal Astronomical Society, 459, 2408

Ambikasaran, S., Foreman-Mackey, D., Greengard, L., Hogg, D. W., & O'Neil, M. 2016, IEEE T. Pattern. Anal., 38, 252

Armitage, P. J., Eisner, J. A., & Simon, J. B. 2016, The Astrophysical Journall, 828, L2

Asplund, M., Grevesse, N., Sauval, A. J., & Scott, P. 2009, Annual Review of Astron and Astrophys, 47, 481

Baruteau, C., Crida, A., Paardekooper, S.-J., et al. 2014, Protostars and Planets VI, 667

Birnstiel, T., Klahr, H., & Ercolano, B. 2012, Astronomy & Astrophysics, 539, A148

Bolmont, E., Raymond, S. N., Leconte, J., Hersant, F., & Correia, A. C. M. 2015, Astronomy and Astrophysics, 583, A116

Bolmont, E., Selsis, F., Owen, J. E., et al. 2017, Monthly Notices of the RAS, 464, 3728

Bouchet, J., Mazevet, S., Morard, G., Guyot, F., & Musella, R. 2013, Physical Review B, 87, 094102

Braak, C. J. F. T. 2006, Statistics and Computing, 16, 239

Cabrera, J., Csizmadia, S., Lehmann, H., et al. 2014, ApJ, 781, 18

Canup, R. M. & Ward, W. R. 2006, Nature, 441, 834

Carrera, D., Johansen, A., & Davies, M. B. 2015, Astronomy & Astrophysics, 579, A43

Chambers, J. E. 1999, The Monthly Notices of the Royal Astronomical Society, 304, 793

Claret, A. & Bloemen, S. 2011, Astronomy & Astrophysics, 529, A75

Connolly, J. 2009, Geochemistry, Geophysics, Geosystems, 10

Cossou, C., Raymond, S. N., Hersant, F., & Pierens, A. 2014, A&A, 569, A56

de Wit, J., Wakeford, H. R., Gillon, M., et al. 2016, Nature, 537, 69

Deck, K. M. & Agol, E. 2015, The Astrophysical Journal, 802, 116

Deck, K. M., Agol, E., Holman, M. J., & Nesvorný, D. 2014, The Astrophysical Journal, 787, 132

Delrez, L., Gillon, M., Triaud, A. H. M. J., et al. 2018, Monthly Notices of the Royal Astronomical Society, sty051

Dittmann, J. A., Irwin, J. M., Charbonneau, D., et al. 2017, Nature, 544, 333

Dorn, C., Venturini, J., Khan, A., et al. 2017, Astronomy & Astrophysics, 597, A37

Drążkowska, J. & Dullemond, C. P. 2014, Astronomy & Astrophysics, 572, A78

Fabrycky, D. C. 2010, ArXiv e-prints [arXiv:1006.3834]

Foreman-Mackey, D., Hogg, D. W., Lang, D., & Goodman, J. 2013, Publications of the Astronomical Society of the Pacific, 125, 306

Fulton, B. J., Petigura, E. A., Howard, A. W., et al. 2017, AJ, 154, 109

Genda, H. & Abe, Y. 2005, Nature, 433, 842

Gillon, M., Demory, B.-O., Benneke, B., et al. 2012, Astronomy & Astrophysics, 539, A28

Gillon, M., Jehin, E., Lederer, S. M., et al. 2016, Nature, 533, 221

Gillon, M., Triaud, A. H. M. J., Demory, B.-O., et al. 2017, Nature, 542, 456

Gimenez, A. & Garcia-Pelayo, J. M. 1983, Ap&SS, 92, 203

Goodman, J. & Weare, J. 2010, Communications in Applied Mathematics and Computational Science, Vol. 5, No. 1, p. 65-80, 2010, 5, 65

Goździewski, K., Migaszewski, C., Panichi, F., & Szuszkiewicz, E. 2016, The Monthly Notices of the Royal Astronomical Society, 455, L104

Grimm, R. E. & McSween, H. Y. 1993, Science, 259, 653

Grimm, S. L. & Stadel, J. G. 2014, The Astrophysical Journal, 796, 23

Güttler, C., Blum, J., Zsom, A., Ormel, C. W., & Dullemond, C. P. 2010, Astronomy & Astrophysics, 513, A56

Hernandez, D. M. & Bertschinger, E. 2015, Monthly Notices of the Royal Astronomical Society, 452, 1934

Holman, M. J. 2005, Science, 307, 1288

Holman, M. J., Fabrycky, D. C., Ragozzine, D., et al. 2010, Science, 330, 51

Howard, A. W., Marcy, G. W., Bryson, S. T., et al. 2012, The Astrophysical Journal Supp., 201, 15

Howell, S. B., Sobeck, C., Haas, M., et al. 2014, Publications of the Astronomical Society of the Pacific, 126, 398

Izidoro, A., Morbidelli, A., & Raymond, S. N. 2014, The Astrophysical Journal, 794, 11

Izidoro, A., Ogihara, M., Raymond, S. N., et al. 2017, MNRAS, 470, 1750

Johansen, A., Blum, J., Tanaka, H., et al. 2014, Protostars and Planets VI, 547

Jontof-Hutter, D., Lissauer, J. J., Rowe, J. F., & Fabrycky, D. C. 2014, The Astrophysical Journal, 785, 15

Jontof-Hutter, D., Rowe, J. F., Lissauer, J. J., Fabrycky, D. C., & Ford, E. B. 2015, Nature, 522, 321

Kopparapu, R. K., Ramirez, R., Kasting, J. F., et al. 2013, Astrophysical Journal, 765, 131

Kopparapu, R. k., Wolf, E. T., Haqq-Misra, J., et al. 2016, Astrophysical Journal, 819, 84

Lambrechts, M. & Johansen, A. 2012, Astronomy & Astrophysics, 544, A32

Lambrechts, M., Johansen, A., & Morbidelli, A. 2014, Astronomy & Astrophysics, 572, A35

Lissauer, J. J. 2007, The Astrophysical Journal Letters, 660, L149

Lithwick, Y., Xie, J., & Wu, Y. 2012, The Astrophysical Journal, 761, 122

Lodders, K. 2003, The Astrophysical Journal, 591, 1220

Luger, R., Sestovic, M., Kruse, E., et al. 2017, Nature Astronomy, 1, 0129

Mandel, K. & Agol, E. 2002, The Astrophysical Journal Letters, 580, L171

Matsumoto, Y., Nagasawa, M., & Ida, S. 2012, Icarus, 221, 624

Mayor, M., Marmier, M., Lovis, C., et al. 2011, ArXiv e-prints

Mills, S. M., Fabrycky, D. C., Migaszewski, C., et al. 2016, Nature, 533, 509

Morbidelli, A., Lambrechts, M., Jacobson, S., & Bitsch, B. 2015, Icarus, 258, 418

Neron de Surgy, O. & Laskar, J. 1997, Astronomy and Astrophysics, 318, 975

Nesvorný, D. & Vokrouhlický, D. 2014, ApJ, 790, 58

Ogihara, M. & Ida, S. 2009, The Astrophysical Journal, 699, 824

Ormel, C. W. & Klahr, H. H. 2010, Astronomy & Astrophysics, 520, A43

Ormel, C. W., Liu, B., & Schoonenberg, D. 2017, A&A, 604, A1

Quarles, B., Quintana, E. V., Lopez, E., Schlieder, J. E., & Barclay, T. 2017, The Astrophysical Journal Letters, 842, L5

Raymond, S. N., Barnes, R., & Mandell, A. M. 2008, The Monthly Notices of the Royal Astronomical Society, 384, 663

Raymond, S. N., Mandell, A. M., & Sigurdsson, S. 2006, Science, 313, 1413

Raymond, S. N., Scalo, J., & Meadows, V. S. 2007, The Astrophysical Journal, 669, 606

Rogers, L. A. 2015, ApJ, 801, 41

Schneider, J., Dedieu, C., Le Sidaner, P., Savalle, R., & Zolotukhin, I. 2011, Astronomy and Astrophysics, 532, A79

Schoonenberg, D. & Ormel, C. W. 2017, Astronomy & Astrophysics, 602, A21

Seager, S., Kuchner, M., Hier-Majumder, C., & Militzer, B. 2007, The Astrophysical Journal, 669, 1279

Seager, S. & Mallén-Ornelas, G. 2003, The Astrophysical Journal, 585, 1038

Southworth, J. 2011, MNRAS, 417, 2166

Spencer, J. R., Rathbun, J. A., Travis, L. D., et al. 2000, Science, 288, 1198

Storn, R. & Price, K. 1997, J. Global Optim., 11, 341

Tamayo, D., Rein, H., Petrovich, C., & Murray, N. 2017a, The Astrophysical Journall, 840, L19

Tamayo, D., Rein, H., Petrovich, C., & Murray, N. 2017b, The Astrophysical Journal Letters, 840, L19

Terquem, C. & Papaloizou, J. C. B. 2007, The Astrophysical Journal, 654, 1110

Turbet, M., Bolmont, E., Leconte, J., et al. 2017, ArXiv e-prints [arXiv:1707.06927]

Unterborn, C. T., Desch, S. J., Hinkel, N., & Lorenzo, A. 2017, ArXiv e-prints

Van Grootel, V., Fernandes, C. S., Gillon, M., et al. 2018, ApJ, 853, 30

Vazan, A., Kovetz, A., Podolak, M., & Helled, R. 2013, Monthly Notices of the Royal Astronomical Society, 434, 3283

Vrugt, J. A., Ter Braak, C., Diks, C., et al. 2009, International Journal of Nonlinear Sciences and Numerical Simulation, 10, 273

Waldmann, I. P., Tinetti, G., Rocchetto, M., et al. 2015, Astrophysical Journal, 802, 107

Wang, S., Wu, D.-H., Barclay, T., & Laughlin, G. P. 2017, ArXiv e-prints

Ward, W. R. 1997, Icarus, 126, 261

Wisdom, J. & Hernandez, D. M. 2015, Monthly Notices of the Royal Astronomical Society, 453, 3015

Wordsworth, R. D., Forget, F., Selsis, F., et al. 2010, Astronomy and Astrophysics, 522, A22

Youdin, A. N. & Goodman, J. 2005, The Astrophysical Journal, 620, 459

Appendix A: Transit timings

Mid-transit time [BJD$_{TDB}$]	uncertainty [days]	Source
2457322.51531	0.00071	TS (Gillon et al. 2016)
2457325.53910	0.00100	TS (Gillon et al. 2016)
2457328.55860	0.00130	TS
2457331.58160	0.00100	TS (Gillon et al. 2016)
2457334.60480	0.00017	VLT (Gillon et al. 2016)
2457337.62644	0.00092	TS (Gillon et al. 2016)
2457340.64820	0.00140	TS (Gillon et al. 2016)
2457345.18028	0.00080	HCT (Gillon et al. 2016)
2457361.79945	0.00028	UK (Gillon et al. 2016)
2457364.82173	0.00077	UK (Gillon et al. 2016)
2457440.36492	0.00020	Sp (Gillon et al. 2017)
2457452.45228	0.00014	Sp (Gillon et al. 2017)
2457463.02847	0.00019	Sp (Gillon et al. 2017)
2457509.86460	0.00210	TS (Gillon et al. 2017)
2457512.88731	0.00029	HST (de Wit et al. 2016)
2457568.78880	0.00100	TS (Gillon et al. 2017)
2457586.91824	0.00064	TS (Gillon et al. 2017)
2457589.93922	0.00092	TS (Gillon et al. 2017)
2457599.00640	0.00021	UK (Gillon et al. 2017)
2457602.02805	0.00071	UK (Gillon et al. 2017)
2457612.60595	0.00085	TN (Gillon et al. 2017)
2457615.62710	0.00160	TS (Gillon et al. 2017)
2457624.69094	0.00066	TN (Gillon et al. 2017)
2457645.84400	0.00110	WHT (Gillon et al. 2017)
2457651.88743	0.00022	Sp (Gillon et al. 2017)
2457653.39809	0.00026	Sp (Gillon et al. 2017)
2457654.90908	0.00084	Sp (Gillon et al. 2017)
2457656.41900	0.00029	TN+LT (Gillon et al. 2017)
2457657.93129	0.00020	Sp (Gillon et al. 2017)
2457659.44144	0.00017	Sp (Gillon et al. 2017)
2457660.95205	0.00035	Sp (Gillon et al. 2017)
2457662.46358	0.00020	Sp (Gillon et al. 2017)

Table A.1. Planet b. TS/TN stands for TRAPPIST-South/-North, VLT for the Very Large Telescope with the HAWK-I instrument, HCT for the Himalayan Chandra Telescope, UK for UKIRT, Sp for Spitzer with the IRAC instrument, HST for the Hubble Space Telescope with the WFC3 instrument, WHT for the William Herschel Telescope, LT for the Liverpool Telescope, SSO for the Speculoos Southern Observatory.

Mid-transit time [BJD$_{TDB}$]	uncertainty [days]	Source
2457663.97492	0.00070	Sp (Gillon et al. 2017)
2457665.48509	0.00017	Sp (Gillon et al. 2017)
2457666.99567	0.00025	Sp (Gillon et al. 2017)
2457668.50668	0.00030	Sp (Gillon et al. 2017)
2457670.01766	0.00034	Sp (Gillon et al. 2017)
2457671.52876	0.00033	Sp (Gillon et al. 2017)
2457721.38747	0.00035	TN
2457739.51770	0.00059	K2
2457741.02787	0.00055	K2
2457742.53918	0.00058	K2
2457744.05089	0.00061	K2
2457745.56164	0.00072	K2
2457747.07208	0.00085	K2
2457748.58446	0.00087	K2
2457750.09387	0.00089	K2
2457751.60535	0.00082	K2
2457753.11623	0.00075	K2
2457754.62804	0.00077	K2
2457756.13856	0.00060	K2
2457757.64840	0.00089	K2
2457759.15953	0.00073	K2
2457760.67112	0.00082	K2
2457762.18120	0.00073	K2
2457763.69221	0.00071	K2
2457765.20298	0.00077	K2
2457766.71479	0.00055	K2
2457768.22514	0.00103	K2
2457769.73704	0.00064	K2
2457771.24778	0.00091	K2
2457772.75738	0.00075	K2
2457774.26841	0.00080	K2
2457775.77995	0.00058	K2
2457777.28899	0.00099	K2
2457778.80118	0.00062	K2
2457780.31297	0.00068	K2
2457781.82231	0.00145	K2
2457783.33410	0.00071	K2
2457784.84372	0.00068	K2
2457792.39979	0.00110	K2
2457793.90955	0.00064	K2

Table A.2. Continued.

Mid-transit time [BJD$_{TDB}$]	uncertainty [days]	Source
2457795.41987	0.00058	K2
2457796.93134	0.00065	K2
2457798.44211	0.00061	K2
2457799.95320	0.00083	K2
2457801.46314	0.00127	K2
2457802.97557	0.00016	Sp + K2
2457804.48638	0.00053	K2
2457805.99697	0.00016	Sp + K2
2457807.50731	0.00017	Sp + K2
2457809.01822	0.00017	Sp + K2
2457810.52781	0.00110	K2
2457812.04038	0.00020	Sp + K2
2457813.55121	0.00014	Sp + K2
2457815.06275	0.00017	Sp + K2
2457816.57335	0.00011	Sp + K2
2457818.08382	0.00015	Sp
2457819.59478	0.00017	Sp
2457821.10550	0.00020	Sp
2457824.12730	0.00018	Sp
2457825.63813	0.00018	Sp
2457827.14995	0.00012	Sp
2457828.66042	0.00024	Sp
2457830.17087	0.00021	Sp
2457833.19257	0.00018	Sp
2457834.70398	0.00016	Sp
2457836.21440	0.00017	Sp
2457837.72526	0.00014	Sp
2457839.23669	0.00017	Sp
2457917.80060	0.00110	TS
2457923.84629	0.00045	SSO
2457935.93288	0.00023	SSO
2457952.55450	0.00110	TN
2457955.57554	0.00069	TN
2457967.66254	0.00050	SSO
2457973.70596	0.00040	SSO

Table A.3. Continued.

Mid-transit time [BJD$_{TDB}$]	uncertainty [days]	Source
2457282.80570	0.00140	TS (Gillon et al. 2016)
2457333.66400	0.00090	TS (Gillon et al. 2016)
2457362.72605	0.00038	UK (Gillon et al. 2016)
2457367.57051	0.00033	TS+VLT (Gillon et al. 2016, 2017)
2457384.52320	0.00130	TS (Gillon et al. 2016)
2457452.33470	0.00015	Sp (Gillon et al. 2017)
2457454.75672	0.00066	Sp (Gillon et al. 2017)
2457512.88094	0.00009	HST (de Wit et al. 2016)
2457546.78587	0.00075	TS (Gillon et al. 2017)
2457551.62888	0.00066	TS (Gillon et al. 2017)
2457580.69137	0.00031	LT (Gillon et al. 2017)
2457585.53577	0.00250	TN (Gillon et al. 2017)
2457587.95622	0.00054	TS+UK (Gillon et al. 2017)
2457600.06684	0.00036	UK (Gillon et al. 2017)
2457604.90975	0.00063	TS (Gillon et al. 2017)
2457609.75461	0.00072	TS (Gillon et al. 2017)
2457614.59710	0.00130	TS (Gillon et al. 2017)
2457626.70610	0.00110	TS (Gillon et al. 2017)
2457631.55024	0.00056	TN+TS (Gillon et al. 2017)
2457638.81518	0.00048	TS (Gillon et al. 2017)
2457650.92395	0.00023	Sp (Gillon et al. 2017)
2457653.34553	0.00024	Sp (Gillon et al. 2017)
2457655.76785	0.00043	Sp (Gillon et al. 2017)
2457658.18963	0.00024	Sp (Gillon et al. 2017)
2457660.61168	0.00051	Sp (Gillon et al. 2017)
2457663.03292	0.00028	Sp (Gillon et al. 2017)
2457665.45519	0.00025	Sp (Gillon et al. 2017)
2457667.87729	0.00031	Sp (Gillon et al. 2017)
2457670.29869	0.00035	Sp (Gillon et al. 2017)
2457672.71944	0.00081	Sp (Gillon et al. 2017)
2457711.46778	0.00064	TN
2457723.57663	0.00050	TS
2457740.53361	0.00088	K2
2457742.95276	0.00115	K2
2457745.37429	0.00063	K2

Table A.4. Planet c

Mid-transit time [BJD$_{TDB}$]	uncertainty [days]	Source
2457747.79699	0.00056	K2
2457750.21773	0.00096	K2
2457752.64166	0.00093	K2
2457755.05877	0.00165	K2
2457757.48313	0.00066	K2
2457759.90281	0.00058	K2
2457762.32806	0.00081	K2
2457764.74831	0.00072	K2
2457767.16994	0.00125	K2
2457769.59209	0.00081	K2
2457772.01483	0.00100	K2
2457774.43458	0.00081	K2
2457776.85815	0.00102	K2
2457779.27911	0.00089	K2
2457781.70095	0.00072	K2
2457784.12338	0.00054	K2
2457791.38801	0.00064	K2
2457793.81141	0.00079	K2
2457796.23153	0.00052	K2
2457798.65366	0.00082	K2
2457801.07631	0.00084	K2
2457803.49747	0.00020	Sp + K2
2457805.91882	0.00017	Sp + K2
2457808.34123	0.00023	Sp + K2
2457810.76273	0.00019	Sp + K2
2457813.18456	0.00024	Sp + K2
2457815.60583	0.00017	Sp + K2
2457818.02821	0.00020	Sp
2457820.45019	0.00022	Sp
2457822.87188	0.00021	Sp
2457825.29388	0.00022	Sp
2457827.71513	0.00022	Sp
2457830.13713	0.00026	Sp
2457832.55888	0.00015	Sp
2457834.98120	0.00025	Sp
2457837.40280	0.00017	Sp
2457839.82415	0.00031	Sp

Table A.5. Continued.

Mid-transit time [BJD$_{TDB}$]	uncertainty [days]	Source
2457560.79730	0.00230	TS (Gillon et al. 2017)
2457625.59779	0.00078	WHT (Gillon et al. 2017)
2457641.79360	0.00290	TS (Gillon et al. 2017)
2457645.84360	0.00210	TS (Gillon et al. 2017)
2457653.94261	0.00051	Sp (Gillon et al. 2017)
2457657.99220	0.00063	Sp (Gillon et al. 2017)
2457662.04284	0.00051	Sp (Gillon et al. 2017)
2457666.09140	0.00160	Sp (Gillon et al. 2017)
2457670.14198	0.00066	Sp (Gillon et al. 2017)
2457726.83975	0.00029	HST
2457738.99169	0.00160	K2
2457743.03953	0.00180	K2
2457747.08985	0.00145	K2
2457751.14022	0.00195	K2
2457755.18894	0.00155	K2
2457759.24638	0.00225	K2
2457763.28895	0.00150	K2
2457767.33866	0.00190	K2
2457771.39077	0.00260	K2
2457775.44026	0.00125	K2
2457779.48843	0.00190	K2
2457783.54023	0.00240	K2
2457791.64083	0.00135	K2
2457803.79083	0.00049	Sp + K2
2457807.84032	0.00030	Sp + K2
2457811.89116	0.00050	Sp + K2
2457815.94064	0.00030	Sp + K2
2457819.99050	0.00050	Sp
2457824.04185	0.00067	Sp
2457828.09082	0.00043	Sp
2457832.14036	0.00037	Sp
2457836.19171	0.00042	Sp
2457961.73760	0.00130	SSO+TS
2457969.83708	0.00068	SSO
2457973.88590	0.00066	SSO

Table A.6. Planet d

Mid-transit time [BJD$_{TDB}$]	uncertainty [days]	Source
2457312.71300	0.00270	TS (Gillon et al. 2017)
2457367.59683	0.00037	TS+VLT (Gillon et al. 2016, 2017)
2457611.57620	0.00310	TN (Gillon et al. 2017)
2457623.77950	0.00100	TS (Gillon et al. 2017)
2457654.27862	0.00049	Sp (Gillon et al. 2017)
2457660.38016	0.00078	Sp (Gillon et al. 2017)
2457666.48030	0.00180	TS+LT (Gillon et al. 2017)
2457672.57930	0.00260	TS (Gillon et al. 2017)
2457721.37514	0.00099	TN (Gillon et al. 2017)
2457733.57300	0.00140	TS
2457739.67085	0.00135	K2
2457745.77160	0.00120	K2
2457751.87007	0.00034	HST
2457757.96712	0.00160	K2
2457764.06700	0.00240	K2
2457770.17109	0.00215	K2
2457776.26378	0.00160	K2
2457782.36226	0.00175	K2
2457794.56159	0.00160	K2
2457800.66354	0.00170	K2
2457806.75758	0.00041	Sp + K2
2457812.85701	0.00034	Sp + K2
2457818.95510	0.00030	Sp
2457825.05308	0.00035	Sp
2457831.15206	0.00027	Sp
2457837.24980	0.00025	Sp
2457934.83095	0.00050	SSO+TS
2457940.92995	0.00086	SSO

Table A.7. Planet e

Mid-transit time [BJD$_{TDB}$]	uncertainty [days]	Source
2457321.52520	0.00200	TS (Gillon et al. 2017)
2457367.57629	0.00044	TS+VLT (Gillon et al. 2016, 2017)
2457634.57809	0.00061	TS+LT (Gillon et al. 2017)
2457652.98579	0.00032	Sp (Gillon et al. 2017)
2457662.18747	0.00040	Sp (Gillon et al. 2017)
2457671.39279	0.00072	Sp (Gillon et al. 2017)
2457717.41541	0.00091	TN (Gillon et al. 2017)
2457726.61960	0.00026	TS (Gillon et al. 2017)
2457745.03116	0.00135	K2
2457754.23380	0.00155	K2
2457763.44338	0.00024	HST
2457772.64752	0.00160	K2
2457781.85142	0.00180	K2
2457800.27307	0.00140	K2
2457809.47554	0.00027	Sp + K2
2457818.68271	0.00032	Sp
2457827.88669	0.00030	Sp
2457837.10322	0.00032	Sp
2457956.80549	0.00054	SSO+HST

Table A.8. Planet f

Mid-transit time [BJD$_{TDB}$]	uncertainty [days]	Source
2457294.78600	0.00390	TS (Gillon et al. 2016)
2457356.53410	0.00200	TS (Gillon et al. 2017)
2457615.92400	0.00170	TS (Gillon et al. 2017)
2457640.63730	0.00100	TS (Gillon et al. 2017)
2457652.99481	0.00030	Sp (Gillon et al. 2017)
2457665.35151	0.00028	Sp (Gillon et al. 2017)
2457739.48441	0.00115	K2
2457751.83993	0.00017	HST
2457764.19098	0.00155	K2
2457776.54900	0.00110	K2
2457801.25000	0.00093	K2
2457813.60684	0.00023	Sp + K2
2457825.96112	0.00020	Sp
2457838.30655	0.00028	Sp
2457924.77090	0.00140	SSO+TS
2457961.82621	0.00068	SSO+TS

Table A.9. Planet g

Mid-transit time [BJD$_{TDB}$]	uncertainty [days]	Source
2457662.55467	0.00054	Sp (Gillon et al. 2017; Luger et al. 2017)
2457756.38740	0.00130	K2
2457775.15390	0.00160	K2
2457793.92300	0.00250	K2
2457812.69870	0.00450	K2
2457831.46625	0.00047	Sp
2457962.86271	0.00083	SSO

Table A.10. Planet h